Phase and structural features of tubular halloysite (7 Å)

VICTOR A. DRITS[1,*], BORIS A. SAKHAROV[1] AND STEPHEN HILLIER[2,3]

[1] *Geological Institute, Russian Academy of Science, Pyzhevsky per, D7, Moscow, Russia*
[2] *The James Hutton Institute, Craigiebuckler, Aberdeen AB15 8QH, UK*
[3] *Department of Soil and Environment, Swedish University of Agricultural Sciences (SLU), SE-75007, Uppsala, Sweden*

ABSTRACT: Despite many reviews and original articles, the actual crystal structure of tubular halloysites remains unclear. Analysis of the structural features of defect-free kaolinite, refined by Bish & von Dreele (1989), shows that the ordered $1Tc$ kaolinite structure can be described equally well by the orthogonal layer cell $\{a_0, b_0, \gamma_0\}$ ($\gamma_0 = 90°$) or by two enantiomorphic oblique layer cells $\{a_1, b_1, \gamma_1\}$ and $\{a_2, b_2, \gamma_2\}$, related to each other by a mirror plane. To simulate diffraction effects for tubular halloysite, the parameters and atomic coordinates of the orthogonal layer unit cell and the layer-displacement vectors t_1 and t_2 responsible for formation of the kaolinite enantiomorphs were deduced by transformation of the parameters of the defect-free kaolinite refined by Bish & von Dreele (1989). Modelling X-ray diffraction patterns show that the samples consist of either single, two or three phases, with the number and their structural features depending on the morphology of the particles. Samples formed of prismatic particles consist of halloysite-like structure (HLS), kaolinite-like structure (KLS) and halloysite cylindrical structure (HCS) phases occurring in various proportions. Samples of proper cylindrical tubes consist of a single HCS phase, whilst samples formed by particles having morphologies intermediate between proper cylindrical and well-developed prismatic forms consist of the KLS and HCS phases. The KLS phase is comparable to low-ordered platy kaolinite with identical unit-cell parameters, layer-displacement vectors and arbitrary stacking faults, except that the layer displacements are not random as in kaolinite, but are distributed at R = 1 such that t_1 and t_2 displacements have a strong tendency to be segregated. Structural parameters describing the HLS and KLS phases are identical, but in the HLS phase there is a strong tendency to the regular alternation of the t_1 and t_2 displacements, and the HLS phases do not contain arbitrary stacking faults. A characteristic feature of the three-phase prismatic samples is that the stacking of the layers along the c^* axis is periodic and the layer thicknesses are similar to those of platy kaolinite. In contrast, in the KLS phase formed in samples with particles of intermediate morphologies, the hydrated 10 and 7.25 Å layers are interstratified. The relationship between the structural and morphological features of the coexisting phases suggests a sequence of phase formation from the centre to the surface of halloysite tubes that progresses from the HCS to the HLS *via* the KLS phase. The results of this study demonstrate that all kaolinite and halloysite (7 Å) varieties are built by the same fundamental structural units.

*Email: victor.drits@mail.ru

Kaolin minerals consist of dioctahedral 1:1 layers of $Al_2Si_2O_{10}(OH)_4$ composition. Each layer is formed by one octahedral sheet and one tetrahedral sheet bound together by tetrahedral sheet apical oxygen atoms. The octahedral sheet contains three possible octahedral cation sites differing in the arrangement of OH groups and oxygen atoms, and dioctahedral 1:1 layers are

designated by the letter A, B or C corresponding to the type of vacant site (Bailey, 1963). Kaolin minerals are divided into two groups. The first includes kaolinite, dickite and nacrite in which cohesion of the adjacent layers is related to hydrogen bonding from OH groups on the basal surface of the alumina octahedral sheet and the oxygen atoms of the basal surface of the tetrahedral sheet of the adjacent 1:1 layer. The second group is the halloysite minerals formed by weathering in many soils and as important economic accumulations in deposits of hydrothermal origin (Dixon, 1989; Joussein et al., 2005; Guggenheim, 2015; Keeling, 2015; Churchman et al., 2016; Hillier et al., 2016; Joussein, 2016; Wilson & Keeling, 2016). In contrast to kaolinite, halloysite is typically hydrated. In a fully hydrated state, halloysite interlayers contain two H_2O molecules per unit cell and the thickness of the 1:1 layer plus the interlayer is equal to ~10 Å. Hydrated halloysite is unstable and readily and irreversibly transforms into a dehydrated state with a periodicity along the c^* axis of ~7 Å. It has been recommended to refer to these various states as halloysite (10 Å) and halloysite (7 Å) (Churchman & Carr, 1975).

It is generally accepted that the initial form of halloysite (i.e. at the time of its formation) is halloysite (10 Å) and that partially or fully dehydrated forms have smaller d spacings of the basal reflections as a result of some degree of post-formation dehydration. The other distinct difference between kaolinite and halloysite is that kaolinite consists exclusively of platy particles with hexagonal outlines, whereas halloysite has been described in a wide variety of morphologies, most commonly cylindrical and prismatic tubular, as well as spheroidal forms, although rare Fe-rich platy forms are also known (Joussein et al., 2005; Moon et al., 2015; Churchman et al., 2016; Hillier et al., 2016).

The tubular forms of halloysite attract special attention due to a rapidly expanding range of their applications in a wide variety of technologies (Lvov et al., 2008; Pasbakhsh et al., 2013; Shchukin et al., 2015; Yuan et al., 2015). Moreover, the cylindrical and prismatic tubular forms are the most common particle forms in most halloysite samples (Chukhrov & Zvyagin, 1966; Dixon & McKee, 1974; Bailey, 1990; Guggenheim, 2015; Churchman et al., 2016; Hillier et al., 2016).

Several different models were suggested to explain the factors controlling the various morphological forms of halloysite particles (Bates et al., 1950; Bailey, 1990; Newman et al., 1994; Singh, 1996; Singh & Mackinnon, 1996; Bordallo et al., 2008; Matusik et al., 2009; Kogure et al., 2013).

Recently, an inherent relationship between cylindrical and prismatic forms of hydrated halloysite was suggested by Hillier et al. (2016). Based on systematic relationships between tube form and size and other regularities, they argued that prismatic tubular forms of halloysite are a late stage in a natural growth sequence of tubular forms that evolves from cylindrical to prismatic as tube size increases.

Investigation of individual tubular particles of hydrated and dehydrated halloysite by selected area electron diffraction (SAED) indicates that at least some of the particles or their fragments have a two-layer periodic structure (Honjo et al., 1954; Honjo & Mihama, 1954; Zvyagin, 1964, 1967; Chukhrov & Zvyagin, 1966; Kohyama et al., 1978; Singh & Gilkes, 1992; Guggenheim, 2015). Application of SAED to the structural study of prismatic halloysite particles showed that these particles have a two-layer monoclinic cell with space group Cc (Chukhrov & Zvyagin, 1966) that corresponds to the $2M_1$ polytype (Zvyagin, 1964, 1967). Recently, Kogure et al. (2011, 2013), using high-resolution transmission electron microscopy (HRTEM) and SAED, investigated cylindrical and prismatic forms of halloysite. Analysis of the HRTEM images of cylindrical particles showed that their stacking structure is generally disordered, but ordered fragments with one-layer kaolinite-like periodicity were often observed. In contrast, the prismatic forms of halloysite have two distinguishing features. The SAED patterns obtained from some particles demonstrate the two-layer stacking according to $2M_1$ polytype, but the corresponding HRTEM images indicates that the two-layer periodicity is observed only as local fragments within otherwise-disordered layer stacking.

The information concerning structural features of halloysites obtained from powder X-ray diffraction (XRD) patterns is even less informative. Regardless, of their origin, the XRD patterns of many halloysites (7 Å) lack hkl reflections, suggesting completely random layer stacking in their structure, whereas others contain rather sharp reflections overlapping on two-dimensional hk bands, indicating a partial ordering in the corresponding structures. Kogure et al. (2013) were the first to interpret the XRD pattern of a dehydrated prismatic halloysite using a modelling method. They concluded that the two well-defined peaks at 4.26 and 4.03 Å in the experimental XRD pattern correspond to the strong 021 and 11$\bar{2}$ reflections of the $2M_1$ structure (Chukhrov & Zvyagin, 1966; Zvyagin, 1967). Hillier et al. (2016) carried out a comprehensive study of a representative

collection of halloysite (10 Å) and halloysite (7 Å) by various methods and deduced a correlation matrix for the XRD Cylindrical/Prismatic (CP) index, the infrared (IR) 'OH-stretching band intensity ratio', particle size and adsorption data.

To conclude, one must note that despite many recently published reviews and original articles (Bailey, 1990, 1993; Joussein *et al.*, 2005; Inoue *et al.*, 2012; Kogure *et al.*, 2013; Churchman, 2015; Guggenheim, 2015; Churchman *et al.*, 2016; Hillier *et al.*, 2016; Joussein, 2016), fundamental problems related to the actual crystal structure of halloysites still remain unresolved. One of these problems is the relationship between the structural features of kaolinite and halloysites. Brindley & Robinson (1946, 1948) assumed that halloysites are the end members of a series of minerals ranging from highly crystalline kaolinite at one end to highly disordered halloysite at the other. On the other hand, one of the conclusions of the review of Churchman *et al.* (2016) is that halloysites are structurally different from kaolinite. The main task of the present manuscript is to clarify the relationships between the defect-free structure of kaolinite and the periodic $2M_1$ structure of halloysite of Zvyagin (1967). As such, it is hoped that discussion of this matter will be considered closed. Additionally, by using the relationships determined together with modelling of the experimental XRD patterns of dehydrated tubular halloysite samples, the phases and the structural features of the studied halloysite samples are revealed.

REVIEW AND RELATIONS OF STRUCTURAL FEATURES

Idealized $2M_1$ structure

Zvyagin (1964, 1967) theoretically deduced possible polytype modifications of dioctahedral and trioctahedral 1:1 layers and established their diffraction features. Using SAED, Chukhrov & Zvyagin (1966) discovered that the diffraction features of some prismatic halloysite particles correspond to those of the two-layer polytype $2M_1$. In the symbolic notation developed by Zvyagin (1964, 1967), the idealized two-layer structure is represented by a stacking sequence expressed as $\sigma_3\tau_+ \ \sigma_3\tau_-$ with a monoclinic symmetry and space group *Cc*. In this notation, σ is the intralayer displacement in the (001) projection between the centres of the ditrigonal rings of the lower tetrahedral sheet and the centres of the vacant octahedral in the upper octahedral sheet of the same kaolin 1:1 layer.

The 1:1 layer has an orthogonal unit cell with a_0 and b_0 parameters in which the [100] direction coincides with the layer mirror plane. In this case, σ_3 is equal to $-a_0/6$, while τ_+ and τ_- correspond to the interlayer displacements between the centres of vacant octahedra of a lower 1:1 layer and the centres of the ditrigonal rings of the tetrahedral sheet of an upper 1:1 layer and are equal to $+b_0/6$ and $-b_0/6$, respectively. This stacking sequence is also described as the regular alternation of the layer displacements with $-a_0/6 + b_0/6$ ($\sigma_3\tau_+$) and $-a_0/6 - b_0/6$ ($\sigma_3\tau_-$). Thus, in the projection on the (001) plane, the layer displacement (Guggenheim *et al.*, 2009) for the two-layer structure is $2\sigma_3 + \tau_+ + \tau_-$ $= -2a_0/6 + b_0/6 - b_0/6 = -a_0/3$ and corresponds to a monoclinic unit cell (Zvyagin, 1964, 1967; Chukhrov & Zvyagin, 1966). To summarize, the idealized two-layer structure of halloysite is the ordered interstratification of the kaolinite layers having *Cm* symmetry, identical interlayer displacements along the mirror plane and shifted with respect to each other by $+b_0/6$ and $-b_0/6$, respectively.

Defect-free kaolinite

According to Bookin *et al.* (1989), the layer periodicity of the ordered 1*Tc* kaolinite can be described equally well by the orthogonal layer cell {a_0, b_0, γ_0} ($\gamma_0 = 90°$) as well as by two enantiomorphic oblique cells {a_1, b_1, γ_1} and {a_2, b_2, γ_2}. The oblique cells are related by the actual or pseudo-mirror plane passing through the C-vacant octahedral sites and the centres of the ditrigonal rings of the tetrahedral sheet in the kaolinite layer (Fig. 1). The parameters of the oblique cells related by the mirror plane are those determined experimentally by Bish & von Dreele (1989) for the defect-free kaolinite sample from Keokuk: $a_{1,2} = 5.1554(1)$ Å, $b_{1,2} = 8.9448(2)$ Å, $\gamma_{1,2} = 89.822(2)°$ (Table 1). The mutual arrangements of the right- and left-hand oblique unit cells and the layer displacement vectors t_1 and t_2, which correspond to individual kaolinite enantiomorphs related by the mirror plane, are shown in Fig. 1. Each of the layer displacements t_1 or t_2 forms the same defect-free 1*Tc* kaolinite. Indeed, coexistence of both right- and left-handed micro- and nano-crystals of kaolinite formed by weathering of ancient crust was experimentally visualized by Samotoin (2011).

Along with the oblique layer cells, Fig. 1 shows the orthogonal cell with the a_0 axis coinciding with the actual or pseudo-mirror plane. If the kaolinite layer with the orthogonal unit cell has *Cm* symmetry, then the regular alternation of the layer displacements t_1 and
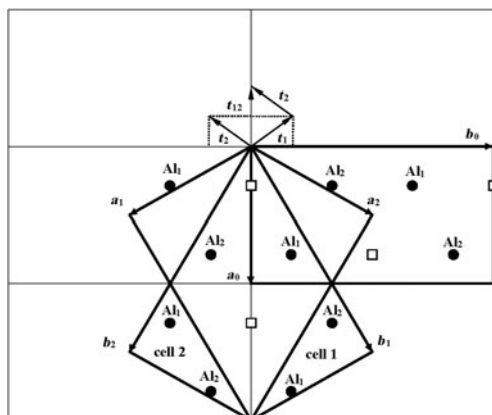
FIG. 1. Mutual arrangement of two-layer oblique unit cells (cell 1 and cell 2) related by a mirror plane passing through the a_0 axis and forming a perpendicular to the b_0 axis of the orthogonal layer unit cell. The layer displacements t_1 and t_2 form the right- and left-handed kaolinite enantiomorphs, respectively, and t_{12} is the layer-displacement vector forming the two-layer periodic halloysite structure.

t_2 are equivalent to the $2M_1$ structure of halloysite. To confirm this proposal, the following operations are required: first, determine layer a_0 and b_0 parameters at $\gamma_0 = 90°$, which satisfy the oblique cell parameters a, b, γ <90° determined for the defect-free kaolinite; second, obtain atomic coordinates in the orthogonal unit cell; and third, demonstrate that a new set of atomic coordinates conforms with the mirror plane.

Transformation from the oblique to orthogonal layer unit cells

As seen in Fig. 1, both oblique cells (cell 1 and cell 2) have the same refined a, b and $\gamma = 89.822°$ parameters and ratio $b/a > \sqrt{3}$ (Table 1). These refined parameters are interrelated with parameters a_0 and b_0 of the idealized orthogonal unit cell (Fig. 2):

$$4a^2 = a_0^2 + b_0^2, 4b^2 = b_0^2 + 9a_0^2 \text{ or } b^2 - a^2 = 2a_0^2 \quad (1)$$

The a_0 and b_0 values were determined from equation 1 using the refined a and b parameters of the oblique cells (Table 1). Note that b/a and b_0/a_0 are interrelated because:

$$b^2/a^2 = (9 + b_0^2/a_0^2)/(1 + b_0^2/a_0^2) \quad (2)$$

Thus, because $b/a > \sqrt{3}$, b_0/a_0 should be $< \sqrt{3}$. In the refined structure of kaolinite (Bish & von Dreele, 1989), the a and b axes of the oblique cell 1 are rotated

clockwise by ~60° with respect to those of the idealized orthogonal unit cell. The latter cell is oriented such that a mirror plane or pseudo-mirror plane of the layer is parallel to the a_0 axis. Figure 2 shows that

$$b_0/a_0 = \tan\gamma_1, b_0/3a_0 = \tan\gamma_2,$$
$$\sin\gamma_1 = b_0/2a, \cos\gamma_1 = a_0/2a, \quad (3)$$
$$\sin\gamma_2 = b_0/2b \text{ and } \cos\gamma_2 = 3a_0/2b$$

where γ_1 and γ_2 correspond to the angles between the a_0, b_0 and a, b axes, and $\gamma = \gamma_1 + \gamma_2$ is the angle between a and b of the oblique cell 1.

To provide a careful correlation between parameters of the refined oblique and orthogonal layer cells, the value of the a parameter is reduced by 1σ and the values of the b and γ values are increased by 1σ (Table 1). After application of equations 1–3, the corrected oblique layer cell parameters ($a = 5.1553$ Å, $b = 8.9450$ Å, $\gamma = 89.825°$) correspond to the orthogonal layer cell parameters with $a_0 = 5.1689$ Å, $b_0 = 8.9214$ Å, $\gamma_0 = 90°$, $b_0/a_0 = 1.7260$ (Table 1). Thus, the refined triclinic oblique layer cell of kaolinite is consistent with the orthogonal two-dimensional layer periodicity.

Fractional atomic coordinates of the orthogonal and oblique unit cells

To determine these relationships, the refined atomic coordinates were transformed from the oblique to the orthogonal coordinate system of the structure. The coordinates of any point in the orthogonal cell, X_0, Y_0, Z_0, and the oblique layer unit cell 1, X, Y, Z (Fig. 2), are related by equation 4:

$$X_0 = X\cos\gamma_1 + Y\cos\gamma_2,$$
$$Y_0 = -X\sin\gamma_1 + Y\sin\gamma_2, \quad (4)$$
$$Z_0 = Z$$

From equation 3, the fractional Cartesian atomic coordinates of the orthogonal x_0, y_0 and oblique x, y cells are related as in equation 5:

$$x_0 = 0.5x + 1.5y, y_0 = -0.5x + 0.5y, z_0 = z \quad (5)$$

Symmetry of the kaolinite layer

The atomic coordinates for the oblique x, y, z and orthogonal x_0, y'_0, z_0 unit cells are given in Table 2. The y coordinate in the orthogonal cell is denoted as y'_0 because Bish & von Dreele (1989) fixed the coordinate origin at the site of the basal oxygen atom O_3 that is located away from the actual or pseudo-

TABLE 1. Refined and corrected parameters of the triclinic kaolinite unit cell transformed into the orthogonal unit cell with the oblique layer unit cell and C1 layer symmetry and transformed into the orthogonal unit cell with the orthogonal layer unit cell and Cm layer symmetry.

	a (Å)	b (Å)	c (Å)	b/a	$\alpha°$	$\beta°$	$\gamma°$	Δx	Δy
Parameters of the triclinic kaolinite unit cell (Bish & von Dreele, 1989)	5.1554(1)	8.9448(2)	7.4048(2)	1.7350	91.7(2)	104.862(1)	89.822(2)	0	0
Corrected parameters of triclinic kaolinite	5.1553	8.9450	7.4048	1.7351	91.7	104.862	89.825	0	0
	a (Å)	b (Å)	h (Å)	b/a	$\alpha°$	$\beta°$	$\gamma°$	Δx	Δy
Parameters of the orthogonal unit cell of kaolinite with oblique layer unit cell, layer symmetry C1	5.1553	8.9450	7.1539	1.7351	90	90	89.825	−0.3683	−0.0239
	a_0 (Å)	b_0 (Å)	h (Å)	b_0/a_0	$\alpha_0°$	$\beta_0°$	$\gamma_0°$	Δx_0	Δy_0
Parameters of the orthogonal unit cell of kaolinite with orthogonal layer unit cell, layer symmetry Cm (right-hand structure)	5.1689	8.9214	7.1539	1.7260	90	90	90.000	−0.2200	0.1722
Parameters of the orthogonal unit cell of kaolinite with orthogonal layer unit cell, layer symmetry Cm (left-hand structure)	5.1689	8.9214	7.1539	1.7260	90	90	90.000	−0.2200	−0.1722

Δx, Δy, Δx_0, Δy_0 = components of layer displacements along a, b or a_0, b_0 axis; h = thickness of the kaolinite layer.
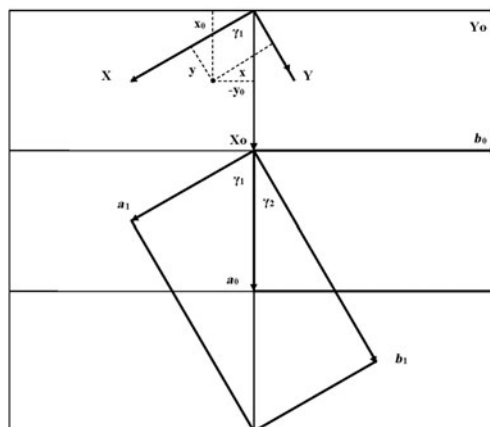

FIG. 2. Oblique cell 1 rotated clockwise by ∼60° with respect to the orthogonal cell and described by a_1, b_1; parameters γ_1 and γ_2 are the angles between the a_0 and a_1 and b_1 axes, respectively. The relationships between the coordinates of any point in the orthogonal, x_0, y_0, z_0, and in the oblique, x, y, z, cells are shown in the upper part of the figure.

mirror plane (Fig. 3). As a result, the y'_0 coordinates of atoms O_4, OH_1 and $(OH)_4$ in the orthogonal cell, which should lie on the mirror plane, are shifted by $0.0156b_0$ from this plane (Fig. 3). Therefore, the orthogonal cell was shifted by −0.0156 along the b_0 axis to appropriately adjust the y_0 coordinates for all atoms in the cell (Table 2). The refined components of the layer displacement along the [100] and [010] directions, −0.3683a and −0.0239b, of the oblique layer cell were transformed using equation 5 into the corresponding components, −0.2200a_0 and 0.1722b_0, of the layer displacement of the orthogonal cell (Table 1).

Analysis of the x_0 and y_0 values in Table 2 shows that there are two sets of atoms. One of them includes O_4, $(OH)_1$ and $(OH)_4$, which have y_0 values very close either to 0 or 0.5. Thus, these atoms are most probably located on the mirror plane, and the layer has *Cm* symmetry. The observed shift of the orthogonal layer cell relative to the mirror plane is caused by the choice of the coordinate origin in the refined kaolinite structure of Bish & von Dreele (1989). In the second group of atomic coordinates, there are pairs of atoms having very similar x_0 and y_0 values, but their y_0 values are of opposite signs (+ or −). Therefore, the absolute values of x_0 and y_0 for each pair were averaged to produce $<x_0>$ and $<y_0>$, which have a direct relation to the refined x and y and to x_0 and y_0. Indeed, the XRD pattern calculated using the corrected oblique layer cell parameters and coordinates x, y, z (Table 2) and that are calculated using the x_0, y_0, z_0

TABLE 2. Transformation atomic coordinates from unit cell of triclinic kaolinite with oblique layer cell to orthogonal layer cells.

Atom	Oblique layer cell			Orthogonal layer cell, C1			Orthogonal layer cell, Cm		
	x	y	z	x_0	y'_0	z_0	$\langle x_0 \rangle$	$\langle y_0 \rangle$	$\langle z_0 \rangle$
Al_1	0.1232	0.4844	0.4721	0.7882	0.1806	0.4721	0.7881	0.1655	0.4710
Al_2	0.6195	0.3188	0.4699	0.7879	−0.15035	0.4699	0.7881	−0.1655	0.4710
Si_1	0.9607	0.3371	0.0909	0.9860	−0.3118	0.0909	0.4844	0.1713	0.0911
Si_2	0.4728	0.1643	0.0913	0.48285	−0.15425	0.0913	0.4844	−0.1713	0.0911
O_1	−0.0666	0.3463	0.3170	0.48615	0.20649	0.3170	0.4838	0.1911	0.3172
O_2	0.0045	0.6528	0.3175	0.98145	0.32415	0.3175	0.4838	−0.1911	0.3172
O_3	0	0.5	0	0.75	0.25	0	0.7492	0.2336	0.0016
O_4	0.1994	0.2299	0.0247	0.44455	0.01525	0.0247	0.4445	0.0001	0.0024
O_5	0.2000	0.7656	0.0032	0.2484	0.2828	0.0032	0.7492	−0.2336	0.0016
$(OH)_1$	−0.0676	0.9621	0.3220	0.4093	0.51485	0.3220	0.4093	0.5	0.3220
$(OH)_2$	0.7421	0.1520	0.6051	0.59990	−0.29505	0.6051	0.5990	−0.3104	0.60655
$(OH)_3$	−0.1891	0.4624	0.6080	0.59990	0.32575	0.6080	0.5990	0.3104	0.60655
$(OH)_4$	0.1910	0.8424	0.6094	0.1681	0.5167	0.6094	0.1683	0.5	0.6094

coordinates and the orthogonal unit cell with *C1* layer symmetry coincide ($R_p = 0.006\%$). On the other hand, these patterns also practically coincide with those calculated using the same orthogonal unit cell but with the atomic coordinates $\langle x_0 \rangle$, $\langle y_0 \rangle$, $\langle z_0 \rangle$ corresponding to *Cm* layer symmetry ($Rp = 1.06\%$ and $Rwp = 1.92\%$). The reason for this is that, for most atoms, the estimated standard deviations determined for the refined atomic positions x, y, z are equal to or greater than the $\langle x_0 \rangle - x_0$, $\langle y_0 \rangle - y_0$ and $\langle z_0 \rangle - z_0$ values, showing that the differences between the atomic coordinates corresponding to the structural models with layer symmetry *Cm* and *C1* are negligible (Table 3). This fact can be considered as a strong argument in support of *Cm* layer symmetry in kaolinite layers.

Relationship of the actual structures of 1Tc kaolinite and 2M₁ halloysite

The transformation of the oblique cell 1 into those of the orthogonal unit cell with *Cm* layer symmetry was repeated for the enantiomorphic cell 2 (Fig. 1). At the same set of atomic coordinates and $\langle x_0 \rangle - x_0$, $\langle y_0 \rangle - y_0$ and $\langle z_0 \rangle - z_0$ values, the layer displacement components, in contrast to cell 1, are equal to $-0.2200a_0$ and $-0.1722b_0$ (Table 1). Thus, to reconstruct the right- and left-hand defect-free kaolinite structure, one must use the same orthogonal unit cell with *Cm* layer symmetry and the $\langle x_0 \rangle$, $\langle y_0 \rangle$, $\langle z_0 \rangle$ atomic coordinates but various layer displacements $t_1 = -0.2200a_0 + 0.1722b_0$ and $t_2 = -0.2200a_0 - 0.1722b_0$, respectively. In contrast, a structure in which the layer-displacement vectors t_1 and t_2 are interstratified regularly as $t_1t_2t_1t\ldots$ has a two-layer periodicity, monoclinic symmetry and space group *Cc*. Indeed, the layer displacement of the structure is $-0.2200a_0 + 0.1722b_0 - 0.2200a_0 - 0.1722b_0 = -0.4400a_0$, $d(001) = 14.3078$ Å because $d(001)$ kaolinite is 7.1539 Å (Bish & von Dreele, 1989) and $\beta = 90° + \arctan(0.44a_0/14.3078) = 99.03°$. Thus, the unit cell parameters of the periodic two-layer structure of halloysite (7 Å) are $a_0 = 5.1689$ Å, $b_0 = 8.9214$ Å, $c = 14.4887$ Å, $\beta = 99.03°$, $\alpha = \gamma = 90°$. The XRD pattern of the structure and the d spacings and *hkl* of the observed reflections are shown in Fig. 4 and Table 4, respectively. To summarize, the t_1 and t_2 layer-displacement vectors have the same length and two fixed directions, each of which is determined by the components of the vector relative to the *a* and *b* parameters of the corresponding oblique cell or to the a_0 and b_0 parameters of the orthogonal unit cell.

The model described above shows that the intralayer displacements of the C-vacant layers are identical and
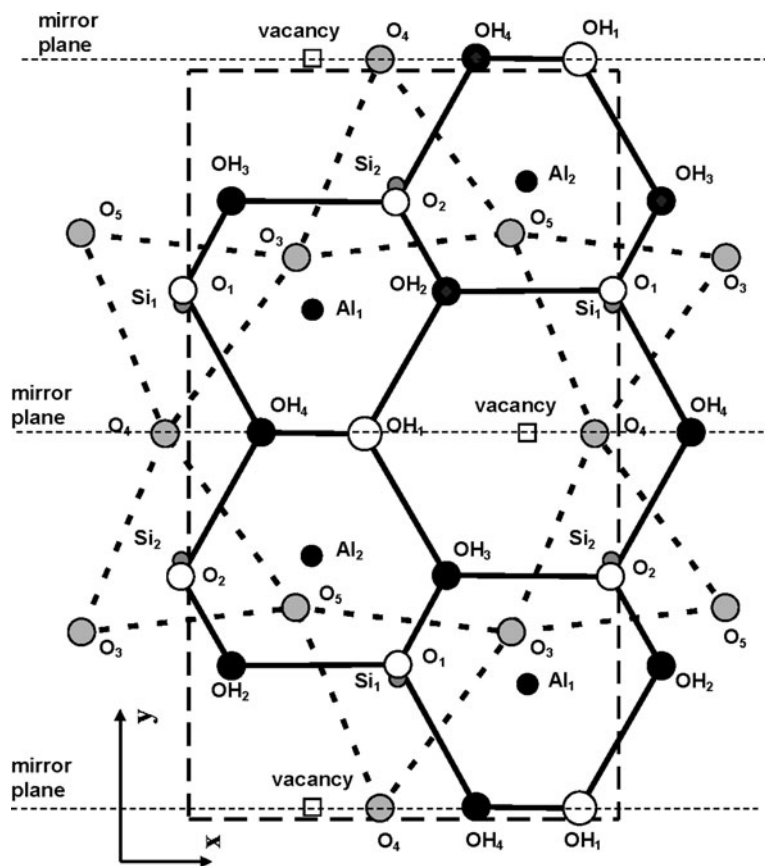
FIG. 3. Mutual arrangement of atoms comprising the kaolinite unit cell in projection on the (001) plane. Coordinates of each atom are given in Table 2. The unit cell chosen by Bish & von Dreele (1989), outlined by the large dashed box, is shifted along the b_0 axis with respect to the mirror plane of the layer.

coincide with the layer mirror plane. Therefore, to obtain the two-layer periodicity, the regular alternation of + $0.1722b_0$ and $-0.1722b_0$ interlayer displacements should occur. A fragment of the periodic two-layer structure in the projection along the a_0 axis is shown in Fig. 5. This shows that both displacements retain identical hydrogen bonds but create electrostatic interactions in adjacent interlayers between the nearest superposing tetrahedral Si cations of the upper layer and octahedral cations (Al_1 or Al_2) of the lower layer, related to each other by the c-glide plane (Fig. 5).

MATERIALS AND METHODS

Samples

Nine samples of tubular halloysites (7 Å) were obtained from occurrences in Russia, the USA and China. Sample Ru-1 is from Olkhon Island, Lake Baikal, Russia, and was formed by weathering of oligoclase (Chekin *et al.*, 1972, 1976). The sample was previously studied by Kogure *et al.* (2013) by XRD, SAED and HRTEM. In cross-sections, the halloysite crystallites displayed various prismatic forms. Sample Ru-3 of halloysite (7 Å) is from the Voznesenskoe fluorite deposit, Priamursk region, Russia, and was described by Chekin *et al.* (1984). Two tubular samples, Col-1 and Col-2 from Wagon Wheel Gap, CO, USA, were obtained from Prof A. Derkowski (Institute of Geological Sciences, Polish Academy of Science, Krakow, Poland). The XRD patterns of two samples, Dragon-actual and Dragon-vs, from the Dragon Mine, UT, USA, were obtained from S. Hillier (The James Hutton Institute, Aberdeen, UK) and hereafter are referred to as Drag-1 and Drag-2. The halloysite (7 Å) specimen from Eureka, NV, USA, obtained from Prof T. Kogure

TABLE 3. Comparison of the estimated standard deviation (e.s.d.) values with the difference between atomic coordinates $<x_0> - x_0$; $<y_0> - y_0$; $<z_0> - z_0$ in which x_0, y_0, z_0 correspond to the $1Tc$ kaolinite structure with $C1$ layer symmetry, whereas $<x_0>$, $<y_0>$, $<z_0>$ correspond to the same triclinic kaolinite but with Cm layer symmetry.

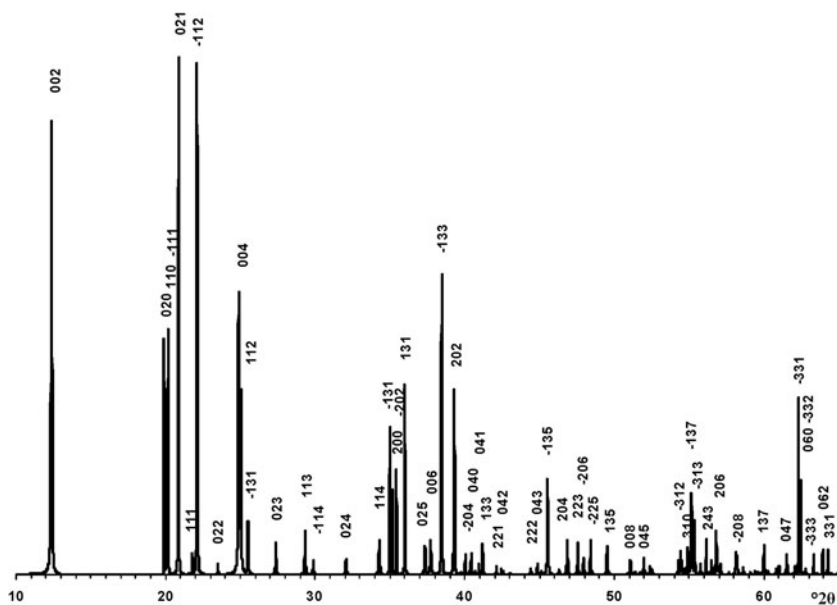| Atom	x-coordinates		y-coordinates		z-coordinates	
	e.s.d. values	$<x_0> - x_0$	e.s.d. values	$<y_0> - y_0$	e.s.d. values	$<z_0> - z_0$
Al_1	0.0015	−0.0001	0.0007	0.0005	0.0010	−0.0011
Al_2	0.0015	0.0001	0.0007	−0.0005	0.0010	0.0010
Si_1	0.0015	−0.0016	0.0006	−0.0014	0.0009	0.0002
Si_2	0.0016	0.0016	0.0006	0.0014	0.0009	−0.0002
O_1	0.0017	−0.0023	0.0009	0.0003	0.0010	0.0002
O_2	0.0017	0.0023	0.0008	−0.0003	0.0010	−0.0002
O_3	0	−0.0008	0	−0.0008	0	0.0016
O_4	0.0015	-5×10^{-5}	0.0008	0.0003	0.0012	0
O_5	0.0015	0.0008	0.0008	−0.0008	0.0012	−0.0016
$(OH)_1$	0.0017	0	0.0008	0.0008	0.0012	0
$(OH)_2$	0.0018	-5×10^{-5}	0.0008	−0.0002	0.0011	0.0014
$(OH)_3$	0.0017	5×10^{-5}	0.0009	0.0002	0.0011	−0.0014
$(OH)_4$	0.0018	0	0.0009	0.0011	0.0012	0

FIG. 4. XRD pattern of the idealized defect-free two-layer structure of halloysite (7 Å). *hkl* indices are indicated above each distinct reflection and *d* values are given in Table 4.

(Department of Earth and Planetary, University of Tokyo, Tokyo, Japan), was studied by Kogure *et al.* (2011) using SAED and HRTEM. Sample Ru-2 is most probably from Russia, but its exact source is unknown. Sample 5-Ch is from the Bifa deposit, Yunnan Province, China, and was described by Hillier *et al.* (2016).

TABLE 4. The *d* spacings and *hkl* of reflections corresponding to the defect-free two-layer periodic structure of halloysite (7 Å).

d-values (Å)	*hkl*	I	*d* values (Å)	*hkl*	I	*d* values (Å)	*hkl*	I
7.154	002	88.4	2.191	133	6.1	1.660	028	10.6
4.461	020	46.2	2.146	221	1.7	1.659	313	
4.431	110	24.1	2.129	042	1.2	1.648	241	2.1
4.405	11$\bar{1}$	48.1	2.123	22$\bar{3}$	0.6	1.638	24$\bar{3}$	6.8
4.259	021	100.0	2.103	026	0.3	1.629	046	2.6
4.078	111	4.1	2.039	222	1.2	1.621	152	8.6
4.020	11$\bar{2}$	99.5	2.020	043	2.0	1.620	206	
3.785	022	2.2	2.010	22$\bar{4}$	0.8	1.615	15$\bar{3}$	1.5
3.577	004	54.9	1.992	13$\bar{5}$	18.8	1.613	31$\bar{4}$	2.0
3.556	112	36.2	1.960	11$\bar{7}$	0.8	1.599	242	0.5
3.492	11$\bar{3}$	10.3	1.939	204	6.6	1.586	20$\bar{8}$	4.5
3.258	023	6.1	1.912	223	6.1	1.585	118	3.6
3.046	113	8.4	1.897	20$\bar{6}$	3.3	1.575	312	1.4
2.989	11$\bar{4}$	2.8	1.880	22$\bar{5}$	6.7	1.563	153	0.5
2.791	024	3.0	1.841	135	5.5	1.555	15$\bar{4}$	0.7
2.615	114	6.8	1.788	008	2.8	1.551	31$\bar{5}$	0.5
2.565	13$\bar{1}$	28.8	1.778	224	0.5	1.541	137	5.6
2.552	200	16.5	1.767	117	0.4	1.535	243	0.8
2.533	20$\bar{2}$	20.2	1.759	045	3.1	1.523	226	1.0
2.495	131	36.8	1.746	22$\bar{6}$	1.5	1.518	24$\bar{5}$	1.6
2.409	025	5.5	1.743	11$\bar{8}$	0.9	1.507	047	3.8
2.385	006	6.7	1.691	31$\bar{1}$	2.8	1.494	154	1.7
2.341	13$\bar{3}$	61.8	1.686	312	4.5	1.490	33$\bar{1}$	34.0
2.293	202	35.9	1.684	150	2.8	1.487	33$\bar{2}$	18.1
2.267	115	0.4	1.683	15$\bar{1}$	2.3	1.487	060	
2.251	20$\bar{4}$	4.0	1.679	240	1.1	1.480	31$\bar{6}$	1.1
2.230	040	4.2	1.674	24$\bar{2}$	1.3	1.468	33$\bar{3}$	3.9
2.215	220	0.7	1.671	310	5.3	1.456	062	4.8
2.204	041	2.1	1.665	13$\bar{7}$	16.0	1.449	331	4.8

Experimental XRD data

Random powder XRD patterns of the samples were obtained with a Bruker D8 diffractometer, at 40 kV, 40 mA, in Bragg-Brentano mode with 250 mm goniometer radius, using Cu-*K*α radiation and a graphite monochromator from 10 to 65°2θ with a 0.05°2θ step increment and a count time of 100 s/step.

Modelling of XRD patterns

To simulate diffraction effects for tubular halloysite, the atomic coordinates obtained above for the kaolinite layer having the orthogonal unit cell, *Cm* layer symmetry and the t_1 and t_2 layer displacements were used with the computer program of Sakharov and Naumov, which is based on algorithms described by Drits & Tchoubar (1990). In addition, model structures may contain an arbitrary number of various types of defects and the distribution of the defects may obey an arbitrary value of the short-range order factor R. The XRD patterns were calculated for halloysite structural models for a statistically homogeneous population of crystallites, each of which has a given content of the interstratified layer-displacement vectors and a set of structural parameters as described above. In the model, the crystallites or coherent scattering domains (CSDs) in the *ab* plane have a disk-like shape and various radii, each of which occurs with equal probability. However, the number of each CSD diameter varies depending on the *hk* diffraction region. To explain the relationships
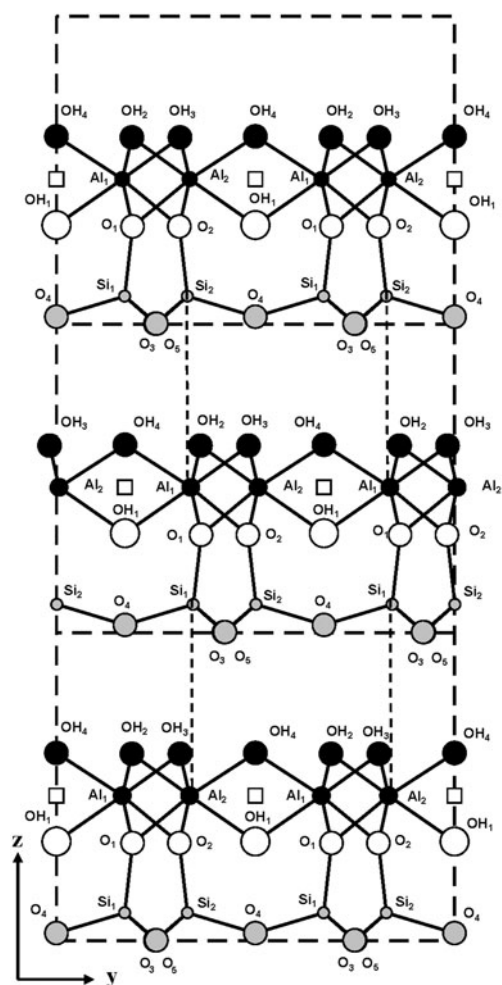
FIG. 5. Fragment of the mutual arrangement of layers of the two-layer periodic halloysite structure in the projection along the a_0 axis. Vertical dashed lines demonstrate the superposition of the tetrahedral Si cations of the upper layer on the octahedral Al cations of the lower layer.

morphological variability of the particles. The positions of the *hkl* reflections in the XRD pattern from a structure composed of layers containing this type of crystalline defect should coincide with those of a layer structure composed of layers with perfectly regular distributions of atoms. However, the widths of *hkl* reflections of the defective layer structure should be increased with corresponding increases of *hk* values. Therefore, ranges of the CSD diameters in the studied samples were divided into three groups with various *hk* values: (02,11;20,13), (04,22;31,24,15) and (06,33), for which $3h^2 + k^2$ are varied within 4–12, 16–28 and 36, respectively. The ranges of the CSD diameters for the second and third groups were decreased by excluding the maximum diameter of the CSDs in the preceding group. The CSD thicknesses were distributed log-normally along the c^* axis and parameters were determined using the mean thickness of CSD, equal to the mean number of layers, N, multiplied by the layer thickness, and the regression given by Drits *et al.* (1997). Corrections for instrumental factors, such as horizontal and vertical beam divergence, length, width and sample thickness, were made according to the recommendations of Drits *et al.* (1993) and Reynolds (1986). If the layer displacement is not fixed in length, variation of the length around the average value is described by Gaussian distributions, where σ_x, σ_y and σ_z are, respectively, the characteristic widths (in fractions of the unit cell parameters) of the distribution in the a, b and c directions.

Powder XRD patterns from halloysite samples may differ because of variations in relative orientations of halloysite particles. The degree of particle preferred orientation was estimated by the angular parameter α equal to the full width at half maximum of the particle distribution (Drits & Tchoubar, 1990). For each model, two XRD patterns were calculated using Cu-$K\alpha_1$ and Cu-$K\alpha_2$ wavelengths and were summed in the ratio of 2:1, respectively. When the structural parameters for each model are fixed, the program automatically seeks the best agreement (minimum Rp factor) between the experimental and calculated XRD patterns by varying the content of each population in a sample. The same program was used to provide the best possible agreement between the XRD pattern from a sample consisting of a mixture of two phases named as N and M, respectively, and an XRD pattern simulated as a sum of XRD patterns corresponding to the N and M phases. For this case, the content of N and M phases in the studied sample is equal to the contribution of the XRD patterns of the N and M phases in the XRD pattern of the sample.

between the size of the CSD and *hk* regions, one must recall that most dispersed crystallites are subject to small deformations that perturb the regular sequence of their constituent atoms (Guinier, 1964; Drits & Tchoubar, 1990; Sakharov & Lanson, 2013). Hence, their description has to include the fact that the atoms do not occupy positions that are strictly defined with respect to the regular lattice nodes, but are slightly displaced from their ideal positions. Such fluctuations in the positions of atoms within layers is intrinsic to dehydrated tubular halloysite as a result of the

Layer displacements for XRD modelling

Application of the trial-and-error approach showed that the best possible agreement between the experimental and calculated $d(hkl)$ values can be achieved when the layer-displacement vectors t_1 and t_2 within the (001) plane are equal to $-0.2200a_0 + 0.1722b_0$ and $-0.2200a_0 - 0.1722b_0$, which coincide with those deduced above. The *Cm* layer symmetry provides a possibility for a third layer-displacement vector $t_0 = 0.3698a_0$, which is placed along the mirror plane. The lengths of t_1, t_2 and t_0 are equal to each other, and the thickness of the CSD was determined by modelling of the basal reflection profiles. A model of the defective halloysite structure consisting of the same layer type was defined by the probability of t_1, t_2 and t_0 translations W_{t1}, W_{t2} and W_{t0}. The mean and maximum thicknesses of CSD having a log-normal distribution are used as variable parameters.

Statistical distribution of the layer displacements in defective planar structures

The symmetrical arrangement of atoms with respect to a mirror plane in a dioctahedral C-vacant 1:1 layer suggests that the most favourable model for stacking faults in a planar defective kaolin structure is one in which the layer-displacement vectors t_1 and t_2, related to each other by the mirror plane, are interstratified with a short-range order factor, R. The best possible agreement between the experimental and simulated XRD patterns of disordered kaolinite samples was previously obtained for the model in which layer-displacement vectors t_1 and t_2 are interstratified at random (*i.e.* where the occurrence probability of a given type of layer displacement does not depend on the type of the layer displacement of the preceding layer and the short-range order factor R = 0) (Plançon *et al.*, 1989; Kogure & Inoue, 2005; Kogure *et al.*, 2010, 2011; Sakharov *et al.*, 2016). In a more specific case, the type of the following layer displacement depends on the particular layer displacement of the preceding layer and the short-range order factor R = 1. In such a structure, t_1 and t_2 layer displacements are interstratified with their relative contents W_{t1} and W_{t2} and their subsequences in a crystal fully described by four junction probability parameters P_{t1t1}, P_{t1t2}, P_{t2t1} and P_{t2t2}. For example, the P_{t1t2} coefficient denotes the probability for the vector t_2 to follow a preceding vector t_1. Therefore, the occurrence probabilities for pairs t_1t_2 and t_2t_2 or triples $t_1t_2t_1$ and $t_2t_2t_1$ of vectors t_1 and t_2 are equal to $W_{t1}P_{t1t2}$ and $W_{t2}P_{t2t2}$ or $W_{t1}P_{t1t2}P_{t2t1}$ and

$W_{t2}P_{t2t2}P_{t2t1}$, respectively. Similarly, any subsequence of t_1 and t_2 can be calculated. In a structure with R = 1 where the t_1 and t_2 layer displacements occur with equal probability, the probability parameters are related by equations 7:

$$W_{t1} = W_{t2} = 0.5;$$
$$P_{t1t1} + P_{t1t2} = 1;$$
$$P_{t1t2} = P_{t2t1};$$
$$P_{t1t1} = P_{t2t2} \qquad (7)$$

Under such conditions, all junction probability parameters are determined if one of them (*e.g.* P_{t1t1}) is specified. If the t_1 and t_2 layer displacements do not occur with equal probability, the probability parameters are related by equations 8:

$$W_t1 + W_{t2} = 1;$$
$$P_{t1t1} + P_{t1t2} = 1;$$
$$P_{t2t1} + P_{t2t2} = 1;$$
$$W_{t1}P_{t1t2} = W_{t2}P_{t2t1} \qquad (8)$$

Thus, to describe each particular sequence in the structure, where the layer displacements t_1 and t_2 are interstratified with R = 1, two of them (*e.g.* W_{t1} and P_{t1t1}) named as independent probability parameters should be specified (Drits & Tchoubar, 1990; Sakharov & Lanson, 2013). Thus, the studied structural phases are not single phases having three-dimensional periodicity, but are described by a set of parameters that specify the occurrence probabilities of various layer subsequences.

RESULTS

Visual inspection of the diffraction features of the XRD patterns of the samples allow us, using criteria described by Hillier *et al.* (2016), to separate them into two groups, one of which includes 5-Ch, Ru-2 and the Eureka samples consisting of presumably cylindrical tubes, and a second group consisting of primarily prismatic forms (Fig. 6).

Modelling of XRD patterns of halloysite (7 Å) with predominantly cylindrical tubes

Diffraction effects from cylindrical tubes of halloysite. According to Hillier *et al.* (2016), the most obvious difference between cylindrical and prismatic tubes is observed in the 20,13 diffraction region. In particular,
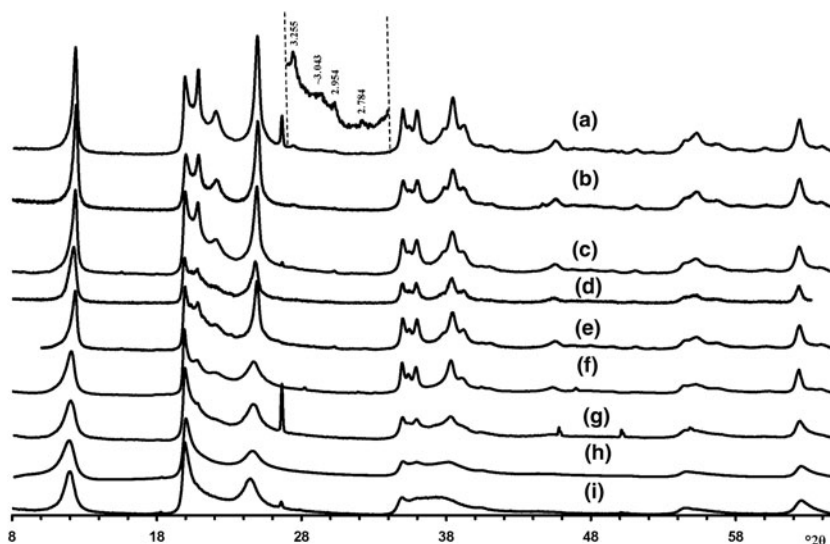
FIG. 6. Experimental XRD patterns of the tubular halloysites (7 Å): (a) Col-1, (b) Drag-2, (c) Ru-1, (d) Drag-1, (e) Col-2, (f) Ru-3, (g) Ru-2, (h) Eureka and (i) 5-Ch.
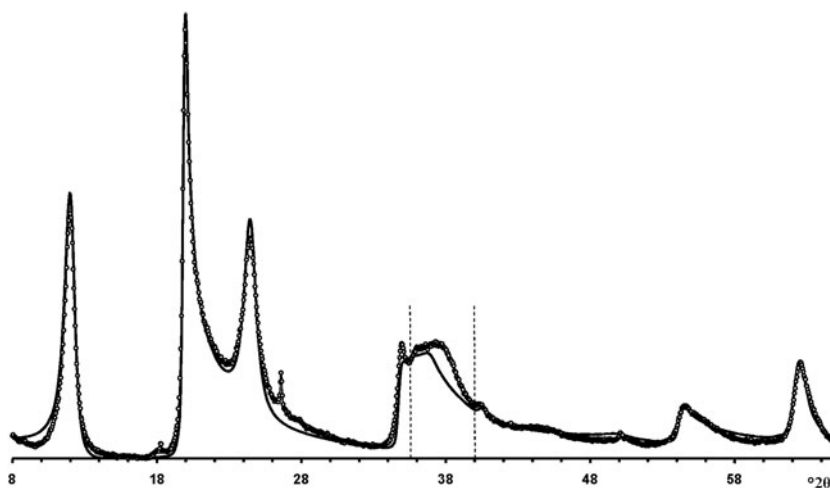

FIG. 7. Comparison of the XRD pattern (dotted line) of sample 5-Ch consisting of cylindrical tubes with those calculated for a planar turbostratic kaolinite structure (solid line). The most significant differences in intensities are observed between the dotted vertical lines at 36–39°2θ.

the 20,13 region of the cylindrical tubes consists of a single broad, slightly rounded maximum with a sharp leading edge, reminiscent of diffraction bands from a two-dimensional turbostratic structure. The XRD pattern of a cylindricalexample (5-Ch) is compared with that calculated for a planar two-dimensional turbostratic kaolinite structure (Fig. 7). In general, these patterns are similar; that is, intensities and profiles for the most distinct maxima coincide, except for intensities in the diagnostic profiles of the broad 20,13 bands within 36–40°2θ (Fig. 7). The varying distribution of the intensities between the compared 20,13 bands is a direct result of the various diffraction effects produced by cylindrical and platy objects.

TABLE 5. Parameters of defective phase KLS and phase contents, W_{KLS} and W_{HCS}, in the Ru-2 and Eureka samples.

Phase	Parameters	Sample Ru-2		Sample Eureka	
		Layer A	Layer B	Layer A	Layer B
KLS	a_0	5.1687 Å	5.1687 Å	5.1687 Å	5.1687 Å
	b_0	8.9217 Å	8.9217 Å	8.9217 Å	8.9217 Å
	h	7.25 Å	10.00 Å	7.26 Å	10.00 Å
	t_1	$-0.2200a + 0.1722b$	–	$-0.2200a + 0.1722b$	–
	t_2	$-0.2200a - 0.1722b$	–	$-0.2200a - 0.1722b$	–
	$W_{At1}:W_{At2}:W_{Bt1}:W_{Bt2}$	0.47:0.47:0.03:0.03		0.475:0.475:0.025:0.025	
	P_{At1At1}, P_{At2Bt1}, P_{At2Bt2}, P_{Bt1At2}, P_{Bt1Bt1}, P_{Bt1Bt2}, P_{Bt2At2}, P_{Bt2Bt1}, P_{Bt2Bt2}	0.60, 0.03, 0.03, 0.47, 0.03, 0.03, 0.47, 0.03, 0.03		0.70, 0.025, 0.025, 0.475, 0.025, 0.025, 0.475, 0.025, 0.025	
	W_a	0.15	1	0.20	1
	σ_z	0.25	0.25	0.3	0.3
	N (mean)	15		10	
	$D\,(hk)$	(02,11,20,13)100–400 Å (04,22,31,24,15)100–300 Å (06,33)100–200 Å		(02,11,20,13)100–300 Å (04,22,31,24,15)100–250 Å (06,33)100–150 Å	
	α	200°		120°	
HCS		Sample 5-Ch			
	$W_{KLS}:W_{HCS}:W_Q$	0.39:0.54:0.07		0.37:0.63:0	
	Rp	9.1%		10.3%	

W_Q = content of quartz.

Therefore, the XRD pattern of the 5-Ch sample can be considered as a standard to account for the contribution of proper cylindrical tubes to the experimental XRD patterns of halloysite samples containing some amount of halloysite cylindrical structure, hereafter termed 'HCS'. In contrast, the 20,13 region from a planar or nearly planar phase will contain at least two distinct individual maxima in addition to the peaked leading edge of the band. In this example (Fig. 7), the intensities and profiles of basal reflections of the planar turbostratic structure were adjusted to those observed in the XRD pattern of the 5-Ch sample.

Sample Ru-2. Modelling of the Ru-2 XRD pattern showed two phases, one of which corresponds to the HCS phase, the other hereafter is referred to as kaolinite-like structure (KLS). One of the most distinct features of the KLS phase is that their layers have various degrees of hydration. Indeed, the first two orders of basal reflections have high and non-rational values of their d spacings equal to 7.348 and 3.611 Å, respectively. The positions and intensities of both reflections were reproduced from the model in which 7.25 and 10.0 Å layer types are interstratified at R = 1

in the ratio 0.94:0.06. Let us denote 7.25 Å layers in the KLS as A_{t1} or A_{t2} and 10 Å layers as B_{t1} or B_{t2} depending on the layer displacement t_1 or t_2 that determines the stacking of the interstratified layers. The parameters of the orthogonal unit cell and the components of the t_1 or t_2 layer displacements along the a_0 and b_0 axes are given in Table 5. The ratio of the layer types is $W_{At1}:W_{At2}:W_{Bt1}:W_{Bt2}$ = 0.47:0.47:0.03:0.03. The values of the independent junction probability parameters controlling the occurrences of various layer pairs such as P_{At1At1}, P_{At2Bt1}, P_{At2Bt2}, *etc.*, are given in Table 5. The occurrences of a full set of the junction probability parameters for all possible layer pairs in matrix form are given in Table 6. Figure 8a compares the 02,11 and 20,13 regions of the experimental XRD pattern with those obtained by summation of the XRD patterns of the KLS and HCS phases. Evidently, the XRD pattern of the HCS phase produces the main contribution to the experimental 02,11 region, whereas the modulated maxima in the experimental 20,13 region are related to the contribution of the KLS phase. Note that some structural features of the studied KLS phase are as follows: first, adjacent layers of the AB or BB layer pairs

TABLE 6. Occurrence of the junction probability parameters for different layer pairs presented in matrix form for samples Ru-2 and Eureka. The different layer pairs are formed by combination of A_{t1}, A_{t2}, B_{t1} and B_{t2} layer types.

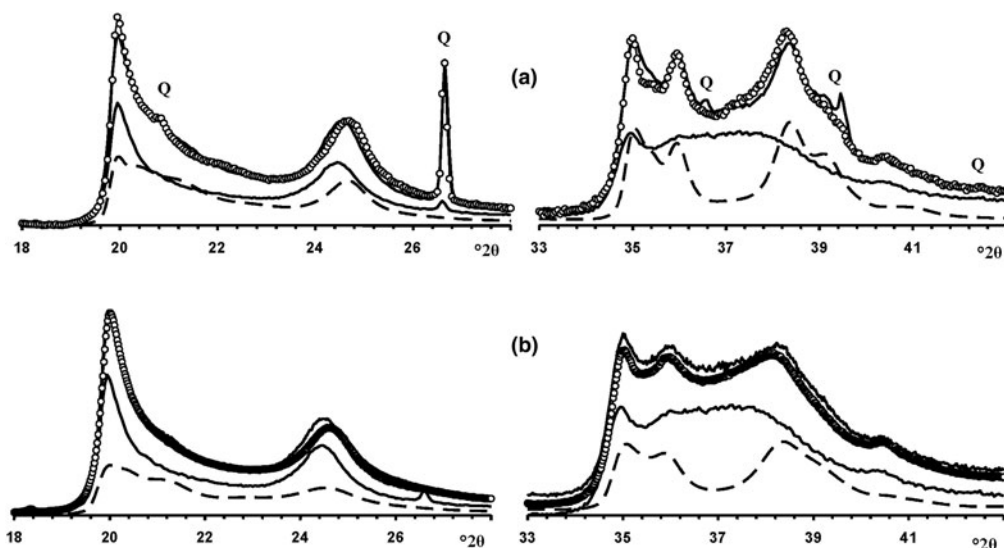| Sample Ru-2	A_{t1}	A_{t2}	B_{t1}	B_{t2}
A_{t1}	0.60	0.34	0.03	0.03
A_{t2}	0.34	0.60	0.03	0.03
B_{t1}	0.47	0.47	0.03	0.03
B_{t2}	0.47	0.47	0.03	0.03
Sample Eureka	A_{t1}	A_{t2}	B_{t1}	B_{t2}
A_{t1}	0.700	0.250	0.025	0.025
A_{t2}	0.250	0.700	0.025	0.025
B_{t1}	0.475	0.475	0.025	0.025
B_{t2}	0.475	0.475	0.025	0.025

FIG. 8. Portions of the experimental XRD patterns of Ru-2 (a) and Eureka (b) samples (dotted lines) corresponding to the 02,11 (left) and 20,13 (right) regions are compared with those obtained by the optimal summation of the XRD patterns of sample 5-Ch (HCS) (solid line) and the KLS phases (dashed line). Q = reflections of quartz impurity.

independently of their particular layer displacement types are shifted with respect to each other in an arbitrary direction by an arbitrary length ($W_a = 100\%$ in Table 5). However, because the total content of 10 Å layers in the KLS phase is only 6%, the contribution of the AB and BB layer pairs to the total diffraction effects from the KLS phase is non-significant. Second, interlayers of the layer pairs AA and AB, independently of their particular layer-displacement vectors, contain 15% of arbitrary stacking faults (for details, see Drits & Tchoubar, 1990). Third, the lengths of the layer thicknesses are varied around the average one along the z-axis according to a Gaussian distribution with characteristic width $\sigma_z = 0.25$. Finally, the most distinguishing structural feature of the KLS phase is that the layer subsequences with identical layer displacement, t_1 or t_2, have a strong tendency to segregation. Indeed, as can be seen in Table 6, $W_{At1} = W_{At2}$ and the
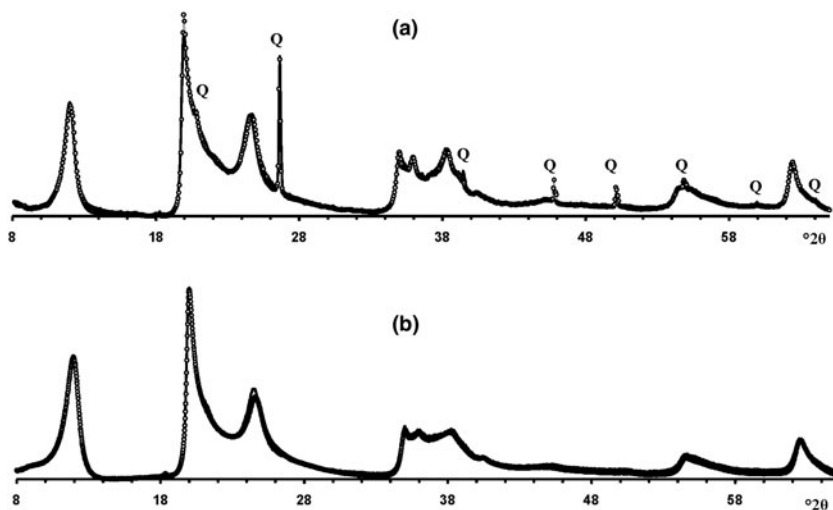
FIG. 9. The best possible agreement between the experimental XRD patterns of samples Ru-2 (a) and Eureka (b) and those obtained by the optimal summation of the XRD patterns of the KLS and HCS phases. Q = reflections of quartz impurity.

values $P_{At1At1} = P_{At2At2} = 0.60$ are significantly higher than those of $P_{At1At2} = P_{At2At1} = 0.34$. This signifies that in the KLS phase the t_1 and t_2 layer displacements are distributed in such a way that instead of their random interstratification, the right- and left-hand kaolinite fragments contain relatively large numbers of identical layer types, A_{t1} or A_{t2}. The optimal agreement between the experimental XRD pattern and that calculated as an optimal sum of the XRD patterns of the KLS and HCS (and a minor impurity of quartz) was obtained at Rp = 9.1% for a phase ratio of 0.39:0.54:0.07 (Table 5, Fig. 9a). The relationships between the CSD diameters and the particular set of *hk* regions are given in Table 5.

Eureka sample. Modelling the Eureka XRD pattern shows that the phase composition and the main structural features are similar to those determined for sample Ru-2 (Table 5, Fig. 8b). Indeed, the sample consists of the same two phases with 7.26 and 10 Å layers interstratified in the ratio 0.95:0.05 so that the ratio of the layer types is $W_{At1}:W_{At2}:W_{Bt1}:W_{Bt2} = $ 0.475:0.475:0.025:0.025 (Table 5). The values of the independent junction probability parameters controlling the occurrence of various layer pairs are given in Table 5 and a full set of such parameters is given in Table 6. As in the KLS phase of sample Ru-2, interlayers in the AA and AB layer pairs, independently of the type of the layer displacement, contain 20% of arbitrary stacking faults. In the BA and BB

layer pairs, the adjacent layers are shifted with respect to each other in an arbitrary direction by arbitrary length ($W_a = 100\%$). In addition, lengths of the layer thicknesses are varied around the averaged one along the z-axis with $\sigma_z = 0.3$. The best agreement between the XRD pattern of the sample and that obtained by the optimal summation of the XRD patterns corresponding to sample 5-Ch and the KLS phase was obtained for the phase ratio equal to 0.63:0.37 at Rp = 10.3% (Fig. 9b). The prevalence of HCS means that the presence of the KLS phase can be noted only by the visible intensity modulations in the 20,13 region of the XRD pattern (Fig. 8b). Table 5 also gives the relationship between CSD diameters and the *hk* regions.

Diffraction effects from prismatic halloysite (7 Å)

Defect-free 1Tc kaolinite to 2M₁ polytype of halloysite via defective kaolinite and halloysite structures. Figure 10 shows calculated XRD patterns for which P_{t1t1} values increase from 0 to 1. The XRD pattern calculated at $P_{t1t1} = 1.0$ corresponds to that of a 1*Tc* kaolinite enantiomorph and contains 11*l*, 02*l* and 20*l*, 13*l* reflections characteristic of its defect-free structure. The structure in which $P_{t1t1} = 0$ corresponds to a perfectly ordered 2*M₁* polytype of halloysite. The interstratification of t_1 and t_2 layer displacements at any P_{t1t1} has a minimal influence on the positions and
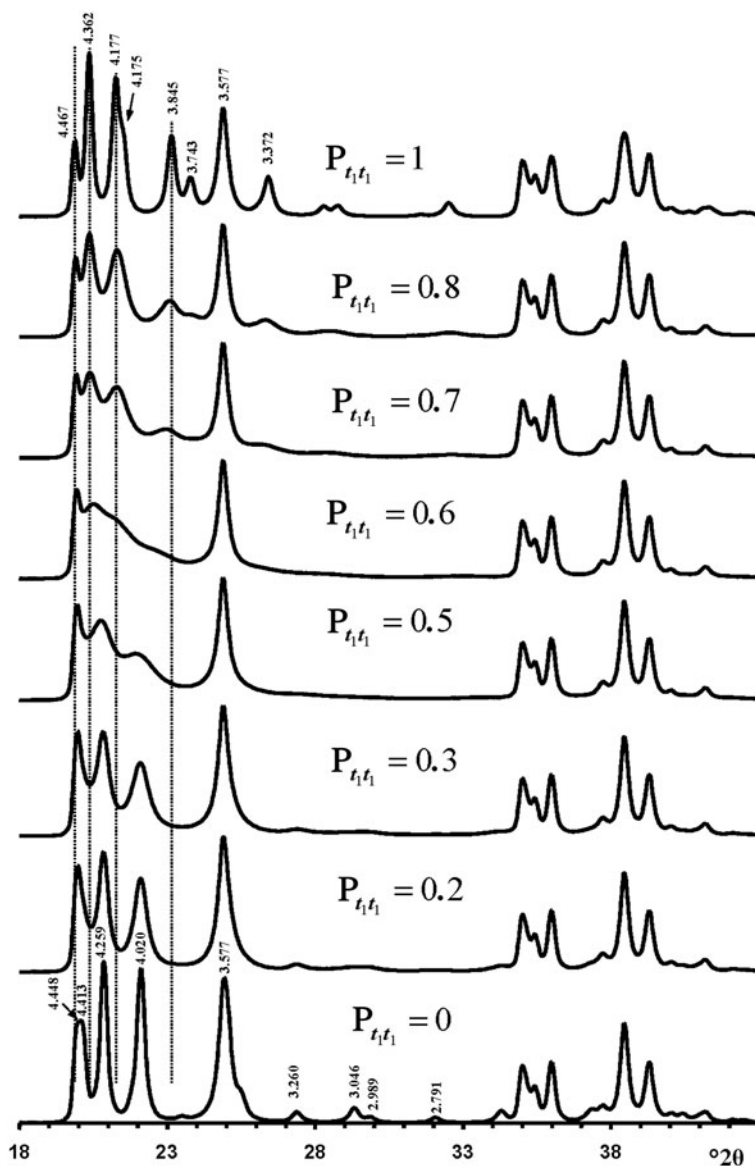
FIG. 10. Evolution of the XRD patterns reflecting a structural transformation from the defect-free kaolinite ($P_{t1t1} = 1$) to the defect-free two-layer periodic halloysite structure $2M_1$ ($P_{t1t1} = 0$) *via* a set of defective halloysite structures calculated at various P_{t1t1} values.

intensity distributions in the diffraction region containing $20l$, $13l$ reflections (Fig. 10). The most distinct feature of the XRD pattern corresponding to $2M_1$ halloysite is the presence of characteristic reflections in the $11l$, $02l$ diffraction region with $d = 4.259$ and 4.020 Å, which were indexed as 021 and $\bar{1}12$ (Zvyagin, 1964, 1967; Chukhrov & Zvyagin, 1966). Remarkably,

these two reflections are reproduced in the XRD patterns within a wide range of P_{t1t1} values varying from 0 to 0.4. Even at the most disordered state corresponding to a completely random interstratification of the t_1 and t_2 layer displacements ($P_{t1t1} = 0.5 = W_{t1}$), two weak and wide maxima are observed at similar positions in the calculated XRD pattern (Fig. 10). Increasing the P_{t1t1}

values from 0 to 0.4 has little influence on the positions of the most intense 020, 021, $11\bar{2}$ reflections, but changes significantly their relative widths and intensities. Indeed, an increase of the P_{t1t1} value decreases the values of P_{t1t2} and P_{t2t1} and increases the proportion of stacking faults due to formation of adjacent layer pairs related to the same layer displacement t_1 or t_2. This is accompanied by a relative decrease of the intensities of the 021 and $11\bar{2}$ reflections with respect to those of the overlapping 020 and 110 reflections (Fig. 10). Similarly, a decrease of P_{t1t1} values from 1.0 to 0.7 also has little effect on the positions of reflections in the 11*l*, 02*l* diffraction regions, but decreases significantly the intensities and increases the widths of the $\bar{1}10$, 110 and $1\bar{1}\bar{1}$, $11\bar{1}$ reflections relative to those of the 020 reflection (Fig. 10).

Furthermore, increasing or decreasing the P_{t1t1} value from 0 and 1.0, respectively, significantly increases the intensity of the diffuse background within the 02*l*, 11*l* diffraction region. Finally, a remarkable feature of the XRD patterns shown in Fig. 10 is that the most intense 021 and $11\bar{2}$ reflections of the ordered and disordered halloysite are located in the middle of the positions of the most intense $1\bar{1}0$, 110 and $1\bar{1}\bar{1}$, $11\bar{1}$ maxima of the ordered and partially disordered kaolinite structures.

Simulation of the experimental XRD patterns of prismatic halloysite

Analysis of the XRD patterns of the samples consisting of prismatic halloysite particles (Fig. 6a–f) has shown that the Drag-2 and Col-2 samples are very similar and that the diffraction features of Drag-1 are intermediate between those of samples Col-1 and Ru-1. Similarly, diffraction features of Ru-3 are intermediate between those of Col-2 and Ru-2. For this reason, the samples from the Dragon Mine and Ru-3 were excluded from the simulation procedure, because their structural features should be intermediate or similar to those determined by modelling of the other halloysite samples.

Sample Col-1. The most distinct feature of the XRD pattern of this sample is that, along with rather strong and narrow 021 and $11\bar{2}$ reflections, it contains a set of very weak reflections whose positions are similar to those of the ordered $2M_1$ halloysite; compare Fig. 10 (P_{t1t1} = 0) and insert in Fig. 6a. At first sight, the pattern indicates a monomineralic halloysite phase and a small amount of quartz. However, a more careful comparison of the XRD pattern with those calculated for the structural models with various P_{t1t1} (Fig. 10) shows – at

least at a qualitative level – that the sample consists of two phases that differ from each other by the nature and content of stacking faults. Indeed, the comparison of the relative intensities of the 020, 021 and $11\bar{2}$ reflections in the experimental XRD pattern with those in the XRD patterns calculated at various P_{t1t1} varying from 0 to 0.4 indicates that the most similar intensity distribution of these reflections is observed in the XRD pattern calculated at P_{t1t1} = 0.2 (Figs 6, 10). Nevertheless, the direct comparison of the experimental XRD pattern and that calculated for the model at P_{t1t1} = 0.2 reveals two distinct features (Fig. 11). First, the relative intensity of the calculated $11\bar{2}$ reflection is much higher than that of the experimental one. Second, the significant background separating individual 020, 021 and $11\bar{2}$ reflections from the baseline of the experimental XRD pattern is probably due to a contribution from a low-ordered population of kaolinite crystallites. As was mentioned above, the strongest reflections of halloysite are located at the midpoint between the positions of the most intense reflections of kaolinite. In addition, decreasing P_{t1t1} values from 1 significantly redistributes the intensities of the 02*l*, 11*l* reflections and increases the background separating these reflections from the baselines of the calculated XRD patterns. Figure 11 compares the experimental XRD pattern corresponding to the 02*l*, 11*l* and 20*l*, 13*l* diffraction regions with that obtained by summation in a 50:50 ratio of the XRD patterns calculated at P_{t1t1} equal to 0.2 and 0.7. This result supports the assumption of a two-phase composition. However, various P_{t1t1} values do not have any influence on the intensities and positions of reflections in the 20*l*, 13*l* diffraction regions (Fig. 11). As a result, the observed difference between experimental and calculated profiles corresponding to the 20*l*, 13*l* diffraction region shows that some additional structural parameters are needed to provide better correlation between the experimental and calculated profiles in this particular region.

The defective structure of each of the coexisting phases in the sample was determined by a trial-and-error method by variation of structural parameters, which influence both the positions and intensities of the coexisting HLS and KLS structural model phases, respectively. The best possible agreement between the experimental and modelled powder XRD patterns of the sample was achieved using a set of parameters that describe the structural models of the HLS and KLS phases (Table 7). Both phases have identical unit cell parameters, *Cm* symmetry of the orthogonal layer cell, the same set of layer displacements and atomic coordinates as given in Tables 1 and 2. Two
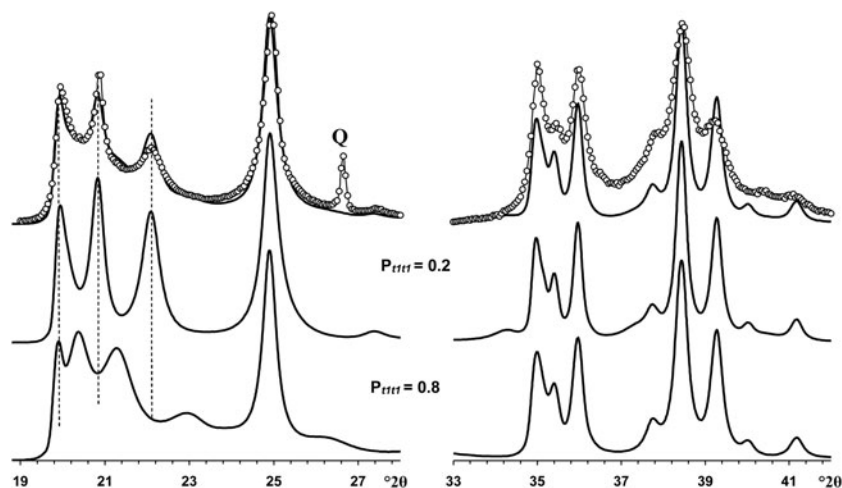
FIG. 11. Portions of the experimental XRD pattern of sample Col-1 (dotted line) corresponding to the 02,11 (left) and 20,13 (right) regions compared with those obtained by summation of the XRD patterns calculated at $P_{t1t1} = 0.2$ and $P_{t1t1} = 0.8$ and taken in the ratio 50:50. Q = reflection of quartz impurity.

characteristic features of the sample should be mentioned: first, the basal reflections of both phases are narrow and form rational series; and second, the thickness of the layers (1:1 layer + interlayer), equal to 7.145 Å, is smaller than those of defect-free and defective kaolinites (7.1575 Å; Sakharov *et al.*, 2016). Indeed, Dixon & McKee (1974), who studied tubular halloysites from Wagon Wheel Gap, CO, USA, also noted that the sharpness of the basal reflections at 7.14 and 3.57 Å of their samples is more characteristic of kaolinite than many halloysites.

In the HLS phase, the t_1 and t_2 layer-displacement vectors occur with the same probability and have the short-range order factor R = 1. The independent probability parameters describing subsequences of the interstratified layer displacements are equal to $P_{t1t1} = P_{t2t2} = 0.2$ and $P_{t1t2} = P_{t2t1} = 0.8$. The complete set of probability parameters is given in Table 8. The particular feature of the HLS phase is that the length of the interlayer displacement varies around the average one along the a_0 axis according to a Gaussian distribution with the characteristic width (in fraction of the a_0 parameter) $\delta_x = 0.06$ (Table 7).

The KLS phase along with the t_1 and t_2 layer displacements contains the third displacement, $t_0 = 0.3698a_0$, which occurs in the relative proportion 0.08 and is interstratified with t_1 and t_2 interlayer-displacement vectors with R = 1. To describe the three-component system, one has to specify each of 12 probability parameters, which are related by

equations 9 (Drits & Tchoubar, 1990; Sakharov & Lanson, 2013):

$$
\begin{aligned}
&P_{t1t1} + P_{t1t2} + P_{t1t0} = 1; \\
&W_{t1} = W_{t1}P_{t1t1} + W_{t2}P_{t2t1} + W_{t0}P_{t0t1}; \\
&W_{t1} + W_{t2} + W_t0 = 1 \\
&P_{t2t1} + P_{t2t2} + P_{t2t0} = 1; \\
&W_2 = W_{t1}P_{t1t2} + W_{t2}P_{t2t2} + W_{t0}P_{t0t2}; \\
&P_{t0t1} + P_{t0t2} + P_{t0t0} = 1; \\
&W_3 = W_{t1}P_{t1t0} + W_{t2}P_{t2t0} + W_{t0}P_{t0t0}, \\
&\text{as } W_{t0} = 0.08, W_{t1} = W_{t2} = 0.46
\end{aligned} \tag{9}
$$

Because of the relations in equations 9, the number of independent junction probability parameters needed to characterize the three-component structural model of the KLS phase is four: $P_{t1t1} = 0.70$, $P_{t0t2} = 0.46$, $P_{t2t0} = P_{t0t0} = 0.08$ – the complete set of probability parameters is given in Table 7. The second feature of the KLS phase is the presence of 10% of arbitrary stacking faults, W_a, which displace adjacent layers in arbitrary directions and lengths within each interlayer (details in Drits & Tchoubar, 1990). The XRD patterns corresponding to the HLS, KLS and quartz phases taken in the ratio 0.46:0.48:0.06, respectively, provides the best agreement of the experimental and calculated XRD patterns at Rp = 11.5%.

In the 02*l*, 11*l* diffraction region (Fig. 12a), the HLS phase contributes significantly to the positions, widths and intensities of the reflections, whereas the KLS

TABLE 7. Simulation parameters of defective phases HLS and KLS and phase contents, W_{HLS}, W_{KLS} and W_{HCS} in the Col-1, Ru-1 and Col-2 samples.

Phase	Parameters	Sample Col-1	Sample Ru-1	Parameters	Sample Col-2
HLS	a_0	5.1687 Å	5.1687 Å	a_0	5.1687 Å
	b_0	8.9217 Å	8.9217 Å	b_0	8.9217 Å
	h	7.145 Å	7.1539 Å	h	7.1539 Å
	t_1	−0.2200a + 0.1722b	−0.2200a + 0.1722b	t_1	−0.2200a + 0.1722b
	t_2	−0.2200a − 0.1722b	−0.2200a − 0.1722b	t_2	−0.2200a − 0.1722b
	t_0	−	−	t_0	0.3698a
	$W_{t1}:W_{t2}$	0.5:0.5	0.5:0.5	$W_{t1}:W_{t2}:W_{t0}$	0.4875:0.4875:0.025
	P_{t1t1}	0.2	0.2	P_{t1t1}; P_{t0t2}; P_{t2t0}; P_{t0t0}	0.25; 0.4875; 0.025; 0.025
	σ_x	0.06	0.10	σ_x	0.08
	N (mean)	12	10	N (mean)	10
	D (hk)	(02,11,20,13)100–500Å (04,22,31,24,15)100–400Å (06,33)100–300Å	(02,11,20,13)100–500 Å (04,22,31,24,15)100–400 Å (06,33)100–300 Å	D (hk)	(02,11,20,13)100–500 Å (04,22,31,24,15)100–450 Å (06,33)100–400 Å
	α	100°	200°	α	200°
KLS	a_0	5.1687 Å	5.1687 Å	a_0	5.1687 Å
	b_0	8.9217 Å	8.9217 Å	b_0	8.9217 Å
	h	7.145 Å	7.1539 Å	h	7.1539 Å
	t_1	−0.2200a + 0.1722b	−0.2200a + 0.1722b	t_1	−0.2200a + 0.1722b
	t_2	−0.2200a − 0.1722b	−0.2200a − 0.1722b	t_2	−0.2200a − 0.1722b
	t_0	0.3698a	0.3698a	t_0	0.3698a
	$W_{t1}:W_{t2}:W_{t0}$	0.46:0.46:0.08	0.475:0.475:0.05	$W_{t1}:W_{t2}:W_{t0}$	0.475:0.475:0.05
	P_{t1t1}; P_{t0t2}; P_{t2t0}; P_{t0t0}	0.70; 0.46; 0.08; 0.08	0.70; 0.475; 0.05; 0.05	P_{t1t1}; P_{t0t2}; P_{t2t0}; P_{t0t0}	0.70; 0.475; 0.05; 0.05
	W_a	0.10	0.15	W_a	0.10
	N (mean)	12	10	N (mean)	12
	D (hk)	(02,11,20,13)100–500 Å (04,22,31,24,15)100–400 Å (06,33)100–300 Å	(02,11,20,13)100–500 Å (04,22,31,24,15)100–400 Å (06,33)100–300 Å	D (hk)	(02,11,20,13)100–500 Å (04,22,31,24,15)100–450 Å (06,33)100–400 Å
	α	100°	200°	α	200°
Two-phase model	$W_{HLS}:W_{KLS}:W_Q$ Rp	0.46:0.48:0.06 11.5%	0.50:0.50:0 10.5%	$W_{HLS}:W_{KLS}$ Rp	0.37:0.63 10.8%
Three-phase model	$W_{HLS}:W_{KLS}:W_{HCS}:W_Q$ Rp	0.51:0.29:0.15:0.05 9.4%	0.46:0.38:0.16:0 8.7%	$W_{HLS}:W_{KLS}:W_{HCS}$ Rp	0.37:0.37:0.26 8.7%

W_Q = content of quartz.

TABLE 8. Completed set of probability parameters characterizing the alternation of layer translations in the Col-1, Ru-1 and Col-2 samples.

Phase	Sample	Col 1	Ru 1	Col 2
			Probability parameters	
HLS	W_{t1}	0.5	0.5	0.4875
	W_{t2}	0.5	0.5	0.4875
	W_{t0}	–	–	0.0250
	P_{t1t1}	0.2	0.2	0.2500
	P_{t1t2}	0.8	0.8	0.7250
	P_{t1t0}			0.0250
	P_{t2t1}	0.8	0.8	0.7250
	P_{t2t2}	0.2	0.2	0.2500
	P_{t2t0}	–	–	0.0250
	P_{t0t1}	–	–	0.4875
	P_{t0t2}	–	–	0.4875
	P_{t0t0}	–	–	0.0250
	W_a	0	0	0
KLS	W_{t1}	0.46	0.475	0.4750
	W_{t2}	0.46	0.475	0.4750
	W_{t0}	0.08	0.050	0.0500
	P_{t1t1}	0.70	0.700	0.7000
	P_{t1t2}	0.22	0.250	0.2500
	P_{t1t0}	0.08	0.050	0.0500
	P_{t2t1}	0.22	0.250	0.2500
	P_{t2t2}	0.70	0.700	0.7000
	P_{t2t0}	0.08	0.050	0.0500
	P_{t0t1}	0.46	0.475	0.4750
	P_{t0t2}	0.46	0.475	0.4750
	P_{t0t0}	0.08	0.050	0.0500
	W_a	0.10	0.150	0.1000

crystallites mostly contribute to the background, to decreasing resolution between adjacent 020, 021 and 11$\bar{2}$ reflections and to the intensity of the 020 reflection. However, in the 20*l*, 13*l* diffraction region, the correlation between the experimental and simulated XRD patterns is not perfect, mostly because of a gap observed between the experimental and simulated intensities from 36.6 to 38.0°2θ (Fig. 12a). This gap is probably related to the presence of the HCS phase because it is exactly in this angular range that the XRD pattern of the HCS phase contains a significantly enhanced intensity in the 20,13 band (Fig. 7). To check this possibility, the experimental XRD patterns were compared with a sum of the XRD patterns of the HLS, KLS and HCS phases. The best agreement between the experimental XRD pattern and that obtained by the optimal summation of the XRD patterns of the coexisting phases was achieved at Rp = 9.4% with a

ratio of 0.51:0.29:0.15:0.05 for the HLS, KLS, HCS and quartz phases, respectively (Figs 13a, 14a). The addition of the HCS phase is accompanied by a significant decrease of the KLS phase (from 0.50 to 0.30) and an increase of the HLS content (from 0.46 to 0.50) – all parameters are given in Table 7.

Sample Ru-1. Modelling of this sample (Fig. 14b) showed that its phase composition is similar to that of sample Col-1. Both samples contain the HLS and KLS phases, which have similar unit cell parameters and layer displacements (Table 7). In both samples, the HLS phases have the same ratio and distribution of the t_1 and t_2 layer displacements, and the length of the interlayer displacement varies around the average one along the a_0 axis with the characteristic width equal to $\delta_x = 0.10$ compared to $\delta_x = 0.06$ for the HLS phase in Col-1 (Table 7). In the KLS phases of both samples,
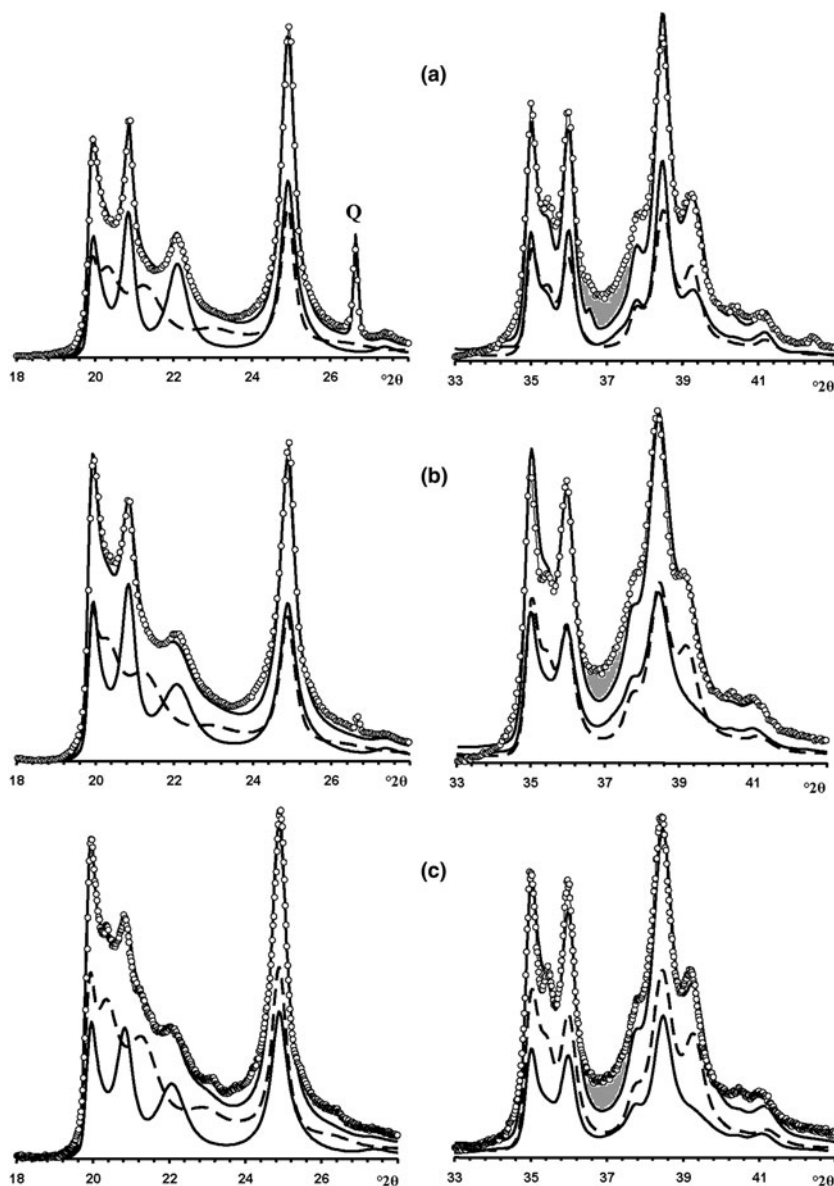
FIG. 12. Portions of the experimental XRD patterns of samples Col-1 (a), Ru-1 (b) and Col-2 (c) (dotted lines) corresponding to the 02,11 (left) and 20,13 (right) regions compared with those (solid lines) obtained by the optimal summation of the XRD patterns of the HLS and KLS phases (lower solid and dashed lines). Dark shaded areas denote the most significant difference between the experimental and calculated intensities observed within 36–39°2θ.

the t_1, t_2 and t_0 layer displacements, occurring in a ratio of 0.475:0.475:0.05, are interstratified with R = 1, and four independent probability parameters ($P_{t1t1} = 0.70$, $P_{t0t2} = 0475$, $P_{t2t0} = P_{t0t0} = 0.05$) in combination with equation 9 fixes the other five values (Table 8). In the KLS phase, the occurrence probability of arbitrary stacking faults is equal to 0.15, compared to 0.10 determined for the KLS phase of Col-1. The XRD patterns corresponding to the HLS and KLS phases taken in equal proportions provided the optimal agreement between the experimental and calculated XRD patterns at Rp = 10.5% (Table 7, Fig. 12b).
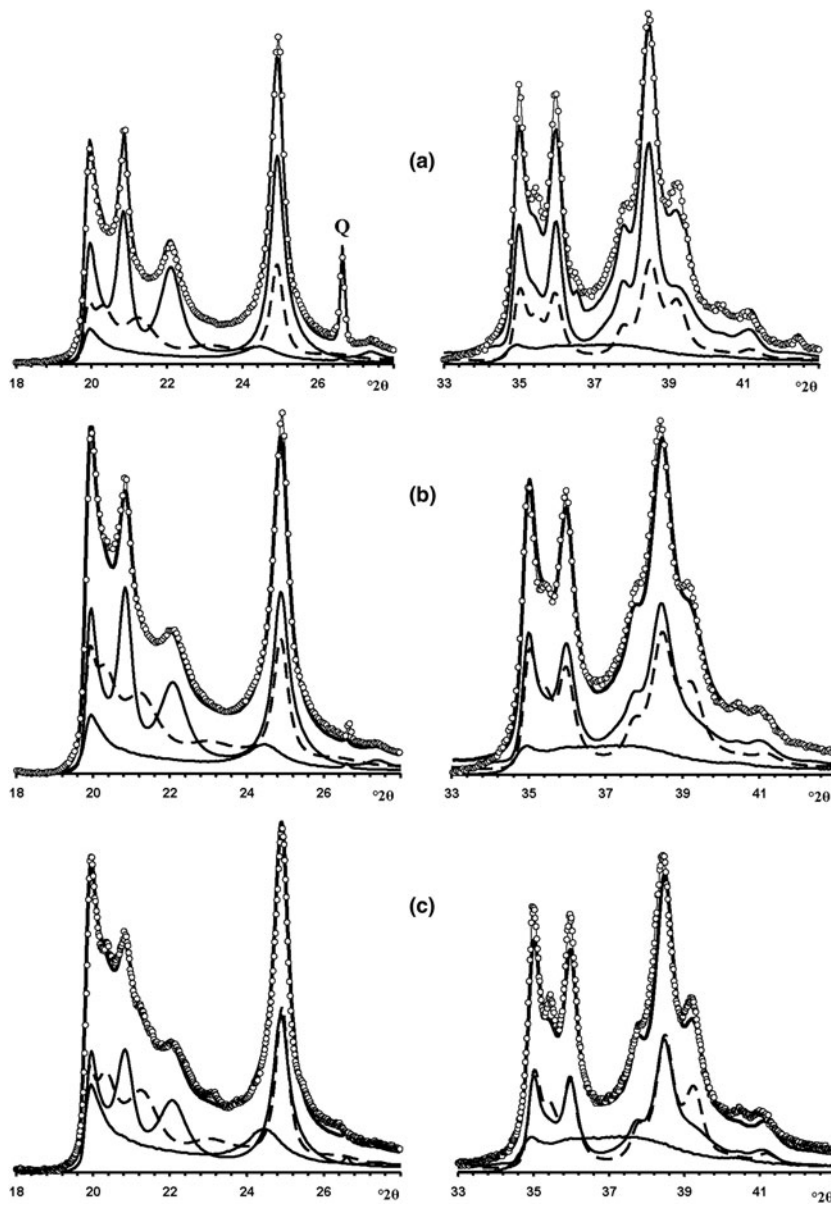
FIG. 13. Fragments of the experimental XRD patterns of samples Col-1 (a), Ru-1 (b) and Col-2 (c) (dotted lines) corresponding to the 02,11 (left) and 20,13 (right) regions compared with those (solid lines) obtained by the optimal summation of the XRD patterns of the HLS, KLS and HCS phases (lower solid and dashed lines).

However, again, the 20,13 region from 36 to 38°2θ shows a gap between the intensities of the XRD pattern and those simulated in terms of the two-phase model. As with sample Col-1, the experimental XRD pattern of the sample was simulated using XRD patterns of the HLS, KLS and HCS phases. The best agreement

between the experimental and simulated XRD patterns was achieved at Rp = 8.7% with the ratio of the coexisting phases equal to 0.46:0.38:0.16 (Table 7, Figs 13b, 14b). As in sample Col-1, the transition from the two-phase to the three-phase model results in a significant decrease of the KLS phase content (from
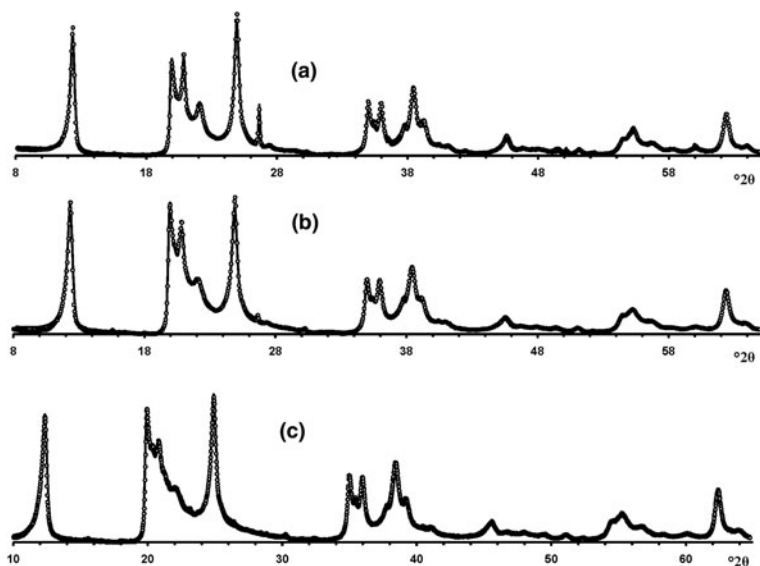
F<small>IG</small>. 14. Best possible agreement between the experimental XRD patterns of samples Col-1 (a), Ru-1 (b) and Col-2 (c) and those calculated by the optimal summation of the XRD patterns of the HLS, KLS and HCS phases.

0.50 to 0.38) with little variation of the HLS phase content (0.46 *vs.* 0.50) (Table 7). The relationship between CSD diameters and the particular set of *hk* regions used for simulation of the XRD pattern is given in Table 7.

Sample Col-2. The main diffraction feature of the XRD pattern of this sample is the further decrease of intensities of the reflections, which are diagnostic of the HLS phase. Nevertheless, the sample contains both HLS and KLS phases, each of which has identical unit cell parameters (Table 7). The HLS phase, in contrast to those described above, contains three layer displacements, t_1, t_2 and t_o, in the ratio 0.4875:0.4875:0.025, interstratified at R = 1. Their distribution is described by four independent probability parameters: $P_{t1t1} = 0.25$, $P_{t0t2} = 0.4875$, $P_{t2t0} = P_{t0t0} = 0.025$ (Table 7), and the complete set of the probability parameters is given in Table 8. In the HLS phase, as in the prismatic samples described above, the length of each interlayer displacement varies around the average one along the a_0 axis with the characteristic width $\delta_x = 0.08$ (Table 7). In the KLS phase of the sample, the t_1, t_2 and t_o layer displacements are interstratified at R = 1 in the ratio 0.475:0.475:0.05 and their distribution is described by four independent probability parameters, $P_{t1t1} = 0.7$, $P_{t0t0} = 0.475$ and $P_{t2t0} = P_{t0t0} = 0.05$, with the amount of arbitrary stacking faults within interlayers equal to 0.10. The complete set of the probability parameters is

given in Table 8. The XRD patterns corresponding to the HLS and KLS phases taken in a ratio of 0.37:0.63, respectively, provides the optimal agreement of the experimental and calculated XRD patterns at Rp = 10.8% (Fig. 12c). The dominating contribution of the KLS phase to the experimental XRD pattern is reflected in the low intensity of the halloysite-like reflections at 4.262 and 4.029 Å (Fig. 12c). Nonetheless, like the previous prismatic samples, a significant discrepancy between intensities of the profiles of the experimental and calculated XRD patterns in the 20*l*, 13*l* diffraction region within 36.4–38.0°2θ (Fig. 12c) shows that the sample contains some of the HCS phase. The optimal summation of the XRD patterns of the HLS, KLS and HCS phases in the ratio 0.37:0.37:0.26 provided the best agreement with the experimental XRD pattern at Rp = 8.7% (Figs 13c, 14c). As with the previous two samples, addition of the HCS phase does not change the HLS content, but the presence of the HCS phase was compensated by a substantial decrease of the KLS phase. Table 7 shows the relationship between the CSD diameter values and the particular set of *hk* regions used for simulation of the XRD pattern.

DISCUSSION

The main aim of this work was to determine the phase composition and structural features of the coexisting phases in halloysite samples having tubular

morphology using an XRD modelling approach. The good agreement between the experimental and calculated XRD patterns obtained for the entire 10–65°2θ diffraction region, with low profile fitting factors (Rp = 8.7–10.3%), is considered strong evidence for the validity of the models (Figs 8–14). The samples investigated consist of either single, two or three phases, and a number of structural features of the coexisting phases depend on the morphology of the particles. The samples formed of prismatic particles consist of the HLS, KLS and HCS phases, populations of proper cylindrical tubes consist of a single HCS phase, whereas those samples formed by particles having morphologies intermediate between proper cylindrical and well-developed prismatic forms consist of the KLS and HCS phases. This may imply that the HLS crystallites were formed on the flat faces of the prismatic tubes. In contrast, the structural features of the KLS phase depend on the particular morphology of the sample. The HCS phase exists in all tubular halloysites, but its content is much lower in the prismatic samples. However, the most significant result of the current work is that the structural models of the coexisting HLS and KLS phases, which provide the good correlation between the experimental and calculated XRD patterns of halloysite (7 Å), were all obtained using the same structural and probability parameters that can be used to describe the defect-free planar kaolinite structure refined by Bish & von Dreele (1989). That is, the studied samples consist of the same (C-vacant) type of layers with the same set of atoms and atomic coordinates, and the layer-stacking arrangements are composed of the same layer-displacement vectors t_1, t_2 and t_0. In other words, kaolinite and halloysite varieties are all built of the same structural units.

Structural similarities and differences between planar and tubular kaolin varieties

Until recently, the relationship between kaolinite and halloysite had remained unclear. For example, in the comprehensive review devoted to the genesis, crystal structure and morphological diversity of halloysite, Joussein *et al.* (2005) noted that the differentiation of halloysite and kaolinite was still problematic and required further special attention. They stated that there is no ideal test to distinguish halloysite from kaolinite in mixtures. More recently, Churchman *et al.* (2016), based on the results of intercalation of halloysite by a set of polar organic molecules, concluded that the intercalation process does not lead to a kaolinite layer stacking, suggesting that halloysites are structurally

different from kaolinite. New insights into the phase composition and structural features of the coexisting phases obtained by simulation of the experimental XRD patterns of the studied samples in combination with the structural features of natural kaolinites (Brindley & Robinson, 1948; Brindley, 1961; Bailey, 1963; Bookin *et al.*, 1989; Plançon *et al.*, 1989; Sakharov *et al.*, 2016) creates an opportunity to propose a more coherent relationship between kaolinite and halloysite (7 Å) structural features.

Planar kaolin varieties. As mentioned previously, kaolinite varieties have either the defect-free or a medium or strongly defective structure. The main source of defects in kaolinite structures is the interstratification of thin enantiomorphic kaolinite fragments that are formed due to the random interstratification of the layer-displacement vectors t_1 and t_2 (Fig. 1). Perfectly ordered kaolinite is of rather rare occurrence and it more commonly forms a physical mixture with a low-ordered kaolinite. Such mixtures are usually referred to as 'well-ordered' kaolinites, but previous modelling of their XRD patterns has shown that the relative content of the high-ordered phase is typically only 25–35% (Plançon *et al.*, 1989; Sakharov *et al.*, 2016). The low-ordered kaolinites along with t_1 and t_2 layer displacements contain up to 5% of the layer-displacement vector t_0, which has the same length as that of the t_1 and t_2 vectors and is oriented along the layer mirror plane. In addition, the interlayer of these kaolinite varieties may contain up to 5% of arbitrary stacking faults (Plançon *et al.*, 1989; Sakharov *et al.*, 2016).

Prismatic kaolin varieties (7 Å). The studied prismatic samples consist of three phases – KLS, HLS and HCS – and their characteristic feature is that the stacking of the layers along the *c** axis is periodic, the layer thicknesses of the coexisting phases are identical for each sample and the values for various samples vary from 7.145 to 7.154 Å (Table 7). The same thickness of layers in each of the coexisting phases present in the studied prismatic samples may indicate that dehydration proceeds more readily to a completely dehydrated structure in the planar layers of prismatic samples.

KLS phase. The structural parameters describing the KLS phase are like those of the low-ordered kaolinite varieties that occur together with defect-free kaolinite. Indeed, both phases have identical unit-cell parameters, layer-displacement vectors and arbitrary stacking faults. However, the content and distribution of

these parameters, at least for the studied KLS phases, differ substantially from those found for low-ordered kaolinite. In the latter, the layer displacements are distributed at random, whereas in the KLS phase found in tubular halloysites, the layer displacements are distributed at R = 1 in such a way that t_1 and t_2 displacements have a strong tendency to be segregated. In other words, the occurrence probabilities for the layer pairs having identical layer displacements t_1t_1 and t_2t_2 are significantly higher than those for layer-displacement fragments t_1t_2 and t_2t_1 (Tables 5, 7). As a result, the partially segregated, rather thick enantio-morphic kaolinite fragments produce well-defined diffraction maxima in the 02,11 region of the XRD patterns of the KLS phase (Figs 9, 11). In further contrast to low-ordered kaolinite, the KLS phase contains a significant content of arbitrary stacking faults increasing up to 10–20% (Tables 5, 7). These stacking faults may be a result of the layer curvature near boundaries with the surfaces of the HCS phase or may appear within the numerous border zones between adjacent faces in the prismatic particles. Their presence significantly modifies the intensity distribution in the 20,13 diffraction regions.

As demonstrated, the best possible agreement between the experimental and calculated XRD patterns was obtained for the model in which both phases (KLS, HLS) of each sample have $W_{t1} = W_{t2}$. This assumption is justified for the HLS phase in which a noticeable tendency to the ordered alternation of the layer-displacement vectors t_1 and t_2 is reasonable. However, the equal content of t_1 and t_2 layer displacements in the KLS phase is not obvious. The most distinct feature of the KLS phase with respect to that of low-ordered kaolinite is a tendency for the same type of layer displacements to be segregated. One can show that this effect depends on both the proportions of the t_1 and t_2 vectors and the occurrence probability parameters P_{t1t1} and P_{t2t2}, controlling the distribution of these vectors in the KLS phase. In particular, almost the same XRD patterns were obtained for the two following models: $W_{t1} = W_{t2} = 0.5$, $P_{t1t1} = 0.7$ and R = 1; and $W_{t1} = 0.7$, $W_{t2} = 0.3$, $P_{t2t2} = 0.5$ and R = 1, because in both models the occurrence probability for layer displacements P_{t1t1} and P_{t2t2} is higher than that for P_{t1t2} and P_{t2t1}.

HLS phase. In our collection, each sample having particles of prismatic shape contains a significant content of the HLS phase. Therefore, in the 02,11 regions, the XRD patterns of the KLS phases are overlapped with those of the HLS phases. As a result, the weak but diagnostic peaks of the KLS phase located between the more intensive maxima of the HLS phase are observed like a background in the experimental XRD patterns of the samples (Figs 11, 12). Structural parameters describing the HLS phase are identical to those describing the KLS phase (Table 7). The main difference between them is in the distributions of the layer displacements. In contrast to the KLS phase in which a tendency to segregation of the same type of layer displacement t_1 or t_2 prevails, in the HLS phase, a tendency to the regular alternation of these displacements dominates. Indeed, as can be seen in Table 8, in the HLS phase, the occurrence probabilities for the layer displacement pairs t_1t_2 and t_2t_1 are higher than those for the layer displacement pairs t_1t_1 and t_2t_2. Another structural feature that is characteristic of the HLS phases is that the length of the interlayer displacement along the a_0 axis varies around the average one and the δ_x values are equal to 0.06–0.10. The most significant difference in the parameters describing the KLS and HLS phases is that the latter phase does not contain arbitrary stacking faults. One possible explanation for this is that the formation of the HLS phase took place in parts of the prismatic particles in which faces were built up by successive planar layers with only a low level of distortion of hydrogen bonds at the boundaries joining adjacent planar faces of the prismatic tubes.

Cylindrical kaolin varieties

Cylindrical tubes are scrolled dioctahedral 1:1 layers having kaolinite composition, and their population forms the HCS phase that is a single representative of halloysite that has no obvious layer-stacking features in common with those of planar kaolinite. Samples consisting of particles having morphologies intermediate between cylindrical and prismatic forms contain the HCS and KLS phases. The most distinct feature of the latter is interstratification of hydrated 10 and 7.25 Å layers. The thickness of 7.25 Å layers is larger than that of layers of the prismatic KLS and HLS phases. Presumably, this signifies that the 7.25 Å layers are not completely dehydrated and their enhanced thickness is related to the presence of some H_2O molecules in their interlayers. The distributions of these molecules within individual interlayers and among various interlayers are presumably heterogeneous. Indirect evidence of partial dehydration of the KLS phase consists of the length of the layer thickness varying around the averaged one along the z-axis with an unusually high value of the Gaussian distribution width, $\sigma_z = 0.25$–0.30 (Table 5). It is possible to assume that the KLS phases in the two-phase samples represent a spectrum of mixed-layer

structures containing various proportions of 10 and 7.20–7.25 Å layers. The layer thickness in the KLS phases being >7.16 Å shows that hydrogen bonding between adjacent layers is weaker, and potentially this creates a favoured ability for such interlayers to expand when the sample is intercalated by certain polar organic molecules (Churchman & Gilkes, 1989).

Which crystallographic direction is preferential for scrolling of halloysite tubes?

Many authors have supposed that, in tubular halloysite, the long axis of the tubes frequently coincides with the *b* axis and only seldom with the *a* axis without specification of these crystallographic directions, or they assume that these directions correspond to those of kaolinite (Bates *et al.*, 1950; Honjo & Mihama, 1954; Chukhrov & Zvyagin, 1966; Zvyagin, 1967; Kohyama *et al.*, 1978; Bailey, 1990; Robertson & Eggleton, 1991; Bobos *et al.*, 2001; Joussein *et al.*, 2005; Churchman *et al.*, 2016). As such, until now the answer to the question as to why and which crystallographic direction is preferential for scrolling of halloysite tubes remained unclear. The results of the present work demonstrate unambiguously that the long axis of tubular halloysite, as a rule, coincides with the b_0 axis of the orthogonal cell. Rolling around this axis preserves the mirror plane within the tube and therefore is accompanied by minimal possible distortion of the halloysite layer structure. The direct evidence of the coincidence of the long axis of halloysite with the b_0 axis follows from the interpretation of the SAED patterns presented by Zvyagin (1964, 1967) and Kogure *et al.* (2013) and simulation of the experimental XRD patterns of the studied samples presented in this work (Fig. 13).

Possible correlation between the evolution of the cylindrical to prismatic morphologies and phase composition and structural features

The phases modelled in the halloysite samples of various known morphologies implies a certain sequence of phase formation from the centre of the halloysite tube to its surface that is from the HCS to HLS through the KLS phases, and we speculate that this sequence correlates to the model of Hillier *et al.* (2016). According to this model, "as the (cylindrical) tubes grow larger it is no longer energetically favourable to compensate misfit between tetrahedral and octahedral sheets by curvature and so at some critical radius other mechanisms common in phyllosilicates generally, such as tetrahedral rotation, presumably come into play.

Consequently, the layers switch from a curved to a planar arrangement such that prismatic tubular forms may be seen as the result of a natural structural progression of tube growth to sizes beyond which the lateral misfit is not comfortably accommodated by curvature." Omitting details, the model of Hillier *et al.* (2016), in general, agrees with variations of the phase composition and structural features of the coexisting phases documented in the present set of samples. First, the good agreement between the experimental and calculated XRD patterns obtained in terms of diffraction effects from planar phyllosilicates is consistent with the formation of planar radial sectors in prismatic halloysite particles. Second, based on the evolution of tubular halloysite particles with their growth, as suggested by Hillier *et al.* (2016), one can reconstruct a sequence of phase formation considering the structural features of the coexisting phases. The first step includes formation of the HCS phase consisting of particles having only cylindrical form. Sample 5-Ch (and similar samples in Hillier *et al.*, 2016) perfectly represents this stage of halloysite formation. During the second step, initial polygonization of the cylindrical tubes takes place and many rather narrow sectors start to form on the tube surface. At this stage, the KLS phase grows on the surfaces of these sectors in proximity to boundaries with the prior formed surfaces of the cylindrical tubes. It is plausible that such layers growing at this stage deviate from the platy (flat) shape and, as a result, the mutual arrangements of the adjacent layers and the corresponding hydrogen bonds are disturbed, leading to the formation of significant amounts of arbitrary stacking faults. These features may be responsible for the fact that the KLS phases are not fully dehydrated and consist of hydrated 10 and 7.25–7.26 Å layers, with the thickness of the latter being greater than that of the completely dehydrated layers of the KLS and HLS phases (7.145–7.154 Å; Tables 5, 7).

In the following stages, with further growth of the larger particles, the content of the KLS phase increases with a consequent relative decrease of the HCS phase content. As a result, a cylindrical form of halloysite is transformed into a prismatic one. It is plausible that, at these stages of morphological transformation, the KLS phases are characterized by a wide spectrum of structural variability. An example of such variability may be illustrated by the tubular halloysite (7 Å) studied by Hillier *et al.* (2016). The 21 samples taken from various countries, formed in various environments and heated at 60°C during spray-drying are characterized by a quite variable range of observed basal spacings of the low-angle basal reflections between 7.325 and 7.607 Å, with

an approximately homogeneous distribution of these values within this interval. It is plausible that the KLS phases of these samples represent a spectrum of mixed-layer structures containing various proportions of 10 and 7.15–7.25 Å layers.

At the final stage of the morphological evolution of halloysite particles, the large prismatic forms were formed with well-developed flat faces. The most distinct structural feature of this stage is formation of the HLS phase with a consistent decrease of the relative content of the HCS phase. It is significant that, in contrast to the KLS phase, the structure of the HLS phase does not contain arbitrary stacking faults, and its layer stacking is controlled mostly by layer-displacement vectors t_1, t_2 and t_0 (Table 7). This may be related to the environment of the layer growth of the HLS taking place on the flat faces of the prismatic crystals. It is plausible that nucleation and layer growth on the flat face occurred in such a way that the adjacent layers in the layer subsequence have an opportunity to be shifted regularly with respect to each other along the b_0 axis by $+0.1722b_0$ and $-0.1722b_0$ to enable the formation of the energetically favourable two-layer structural configuration similar to that shown in Fig. 4. Because the formation of the HLS phase takes place in thermodynamic non-equilibrium conditions, its structure, along with the rather thick structural fragments of the ordered alternation of the t_+ and t_- layer displacements, contains some fragments with a disordered distribution of these displacements. Alternatively, it is perhaps even more plausible that the ordered two-layer periodicity of halloysite is formed in its hydrate state, and this periodicity is inherited though partially disturbed during dehydration. For example, it is pertinent to note that Kohyama *et al.* (1978) observed the two-layer periodic structure in both hydrated and dehydrated halloysite particles.

Correlation between XRD, SAED and TEM data

Among the samples studied in this work, Ru-1 and Eureka, having contrasting morphologies of their particles, were investigated by Kogure *et al.* (2013) and Kogure *et al.* (2011), respectively. The most distinct morphological feature of the particles comprising sample Ru-1 is that their cross-sections displayed prismatic morphology with a small number of faces and acute angles between the adjacent faces. These observations agree with the methodological approach of this work that considers the HLS and KLS phases in terms of planar structural models. The analysis of SAED patterns and HRTEM images has

shown that projections of crystallites along the b_0 axis correspond to the one-layer periodic structure of kaolinite. In contrast, when the incident electron beam was parallel to the a_0 axis, the HRTEM images show, along with almost random interstratification of the t_1 and t_2 layer displacements, the presence of structural fragments with a regular alternation of these displacements corresponding to the two-layer periodic structure. These results agree with the structural models of the HLS and KLS phases determined by modelling of the experimental XRD patterns. According to Kogure *et al.* (2011), the high-resolution scanning electron microscopy images of tubular particles of Eureka samples showed that they have a cylindrical morphology without noticeable polygonization. In agreement with the modelling results, the HRTEM images taken with the incident electron beam perpendicular to the tube or b_0 axis showed that the stacking structure of the sample is generally disordered, but ordered packets with one-layer periodicity, as is found in kaolinite, were observed.

CONCLUSIONS

Modelling of experimental XRD patterns – a method widely applied for the comprehensive structural study of finely dispersed platy phyllosilicates – was used for the first time for the determination of the phase composition and structural features of dehydrated or partially dehydrated halloysite (7 Å) samples with a tubular morphology of their particles. Samples formed of prismatic particles consist of three phases termed HLS, KLS and HCS, the first two of which are planar and the other cylindrical; populations of proper cylindrical tubes form a single HCS phase, whereas the samples formed by particles having morphologies intermediate between cylindrical and well-developed prismatic forms consist of the KLS and HCS phases. The diagnostic structural features of each phase in each morphological group were determined. Good agreement between experimental and calculated XRD patterns with low profile fitting factors (Rp = 8.7–10.3%) is considered strong evidence for the validity of the defined models. Remarkably, structural models of the coexisting HLS and KLS phases were both obtained using the structural and probability parameters describing defect-free planar kaolinite enantiomorphs. Indeed, the studied samples consist of the same (C-vacant) type of layers with the same set of atoms, atomic positions and layer stacking composed of the same layer-displacement vectors t_1, t_2 and t_0 as are found in kaolinite. New insights into the phase

composition and structural features of the coexisting phases obtained by simulation of the experimental XRD patterns provide a significant contribution to one of the fundamental problems related to the actual crystal structure of tubular halloysite varieties. In particular, analysis of the structural features of defective kaolinite and the KLS phase should settle disagreements about the relationship between kaolinite and halloysite. The occurrence of various phases with particular structural features suggests a model for the evolution of the phase formation as a function of the degree of transformation or growth of cylindrical tubes to well-developed prismatic particles. This model correlates with that of the evolution of halloysite particles from cylindrical to prismatic morphologies developed by Hillier *et al.* (2016). The choice of the layer unit cell shows that the long axis of tubular halloysite particles coincides not with the *b* axis of the oblique cell, as was generally accepted, but with the b_0 axis of the orthogonal cell of the defect-free kaolinite; these axes have different orientations and lengths.

ACKNOWLEDGEMENTS

REFERENCES

Bailey S.W. (1963) Polymorphism of the kaolinite minerals. *American Mineralogist*, **48**, 1196–1209.

Bailey S.W. (1990) Halloysite: a critical assessment. Pp. 89–98 in: *Proceedings of the 9th International Clay Conference 1989* (V.C. Farmer & Y. Tardy, editors). Sciences Géologiques, Mémoire 86, Strasbourg, France.

Bailey S.W. (1993) Review of the structural relationships of the kaolin minerals. Pp. 25–42 in: *Kaolin Genesis and Utilization* (H.H. Murray, W.M. Bundy & C.C. Harvey, editors). The Clay Minerals Society, Boulder, CO, USA.

Bates T.F., Hildebrand F.A. & Swineford A. (1950) Morphology and structure of endellite and halloysite. *American Mineralogist*, **35**, 463–484.

Bish D.L. & von Dreele R.B. (1989) Rietveld refinement of non-hydrogen atomic positions in kaolinite. *Clays and Clay Minerals*, **37**, 289–296.

Bordallo H.N., Aldridge L.P., Churchman G.J., Gates W.P., Telling M.T.F., Kiefer K., Fouquet P., Seydel T. & Kimber S.A.J. (2008) Quasi-elastic neutron scattering studies on clay interlayer-space highlighting the effect of the cation in confined water dynamics. *Journal of Physical Chemistry C*, **112**, 13982–13991.

Brindley G.W. (1961) Kaolin, serpentine and kindred minerals. Pp. 51–131 in: *The X-Ray Identification and Crystal Structures of Clay Minerals* (G. Brown, editor). Mineralogical Society, London, UK.

Brindley G.W. & Robinson K. (1946) The structure of kaolinite. *Mineralogical Magazine*, **27**, 242–253.

Brindley G.W. & Robinson K. (1948) X-ray studies of halloysite and metahalloysite. *Mineralogical Magazine*, **28**, 393–406.

Bobos I., Duplay J., Rocha J. & Gomes C. (2001) Kaolinite to halloysite-7Å transformation in the kaolin deposit of Sãovicente de Pereira, Portugal. *Clays and Clay Minerals*, **49**, 596–607.

Bookin A.S., Drits V.A., Plancón A. & Tchoubar C. (1989) Stacking faults in kaolin-group minerals in the light of real structural features. *Clays and Clay Minerals*, **37**, 297–307.

Chekin S.S., Samotoin N.D. & Finko V.I. (1972) Spiral–cylindrical shape and growth of halloysite crystallites. *Izvestiya Akademii Nauk SSSR, Seriya Geologicheskaya*, **6**, 111–124 (in Russian).

Chekin S.S., Samotoin N.D. & Finko V.I. (1976) Formation of halloysite by weathering of oligoclase. *Izvestiya Akademii Nauk SSSR, Seriya Geologicheskaya*, **11**, 88–114 (in Russian).

Chekin S.S., Samotoin N.D. & Finko V.I. (1984) A spiral structure and genesis of prismatic crystals of halloysite (7 Å). *Izvestiya Akademii Nauk SSSR, Seriya Geologicheskaya*, **4**, 74–84 (in Russian).

Chukhrov F.V. & Zvyagin B.B. (1966) Halloysite, a crystallochemically and mineralogically distinct species. Pp. 11–25 in: *Proceedings of the International Clay Conference, Jerusalem, Israel* (L. Heller & A. Weiss, editors). Israel Program for Scientific Translation, Jerusalem, Israel.

Churchman G.J. (2015) The identification and nomenclature of halloysite (a historical perspective). Pp. 51–67 in: *Natural Mineral Nanotubes* (P. Pasbakhsh & G.J. Churchman, editors). Apple Academic Press, Oakville, Ontario, Canada.

Churchman G.J. & Carr R.M. (1975) The definition and nomenclature of halloysites. *Clays and Clay Minerals*, **23**, 382–388.

Churchman G.J. & Gilkes R.J. (1989) Recognition of intermediates in the possible transformation of halloysite to kaolinite. *Clay Minerals*, **24**, 579–590.

Churchman G.J., Pasbakhsh P., Lowe D.J. & Theng B.K.G. (2016) Unique but diverse: some observations on the formation, structure and morphology of halloysite. *Clay Minerals*, **51**, 395–416.

Dixon J.B. (1989) Kaolin and serpentine group minerals. Pp. 467–525 in: *Minerals in Soil Environments* (J.B. Dixon & S.B. Weed, editors). Soil Science Society of America, Madison, WI, USA.

Dixon J.B. & McKee T.R. (1974) Internal and external morphology of tubular and spheroidal halloysite particles. *Clays and Clay Minerals*, **22**, 127–137.

Drits V.A. & Tchoubar C. (1990) *X-Ray Diffraction by Disordered Lamellar Structures*. Springer-Verlag, Berlin, Germany.

Drits V.A., Kameneva M.Y., Sakharov B.A., Dainyak L. G., Tsipursky S.I., Smoliar-Zviagina B.B., Bookin A. S. & Salyn A.L. (1993) *The Actual Structure of Glauconites and Related Mica-like Minerals*. Nauka, Novosibirsk, Russia (in Russian).

Drits V.A., Środoń J. & Eberl D.D. (1997) XRD measurements of mean crystallite thickness of illite and illite/smectite: reappraisal of the Kubler index and the Scherrer equation. *Clays and Clay Minerals*, **45**, 461–475.

Guggenheim S. (2015) Phyllosilicates used as nanotube substrates in engineered materials: structures, chemistries, and textures. Pp. 4–48 in: *Natural Mineral Nanotubes* (P. Pasbakhsh & G.J. Churchman, editors). Apple Academic Press, Oakville, Ontario, Canada.

Guggenheim S., Adams J.M., Bergaya F., Brigatti M.F., Drits V.A., Fromoso M.L.L., Galan E., Kogure T., Stanjek H. & Stucki J.W. (2009) Nomenclature for stacking in phyllosilicates: report of the Association International pour I'Etude des Argiles (AIPEA) nomenclature committee for 2008. *Clay Minerals*, **44**, 157–159.

Guinier A. (1964) Diffraction par les réseaux cristallins imparfaits. Pp. 490–636 in: *Théorie et Technique de la Radiocristallographie*. Dunod, Paris, France.

Hillier S., Brydson R., Delbos E., Fraser T., Gray N., Pendlowski H., Phillips I., Robertson J. & Wilson I. (2016) Correlations among the mineralogical and physical properties of halloysite nanotubes (HNTs). *Clay Minerals*, **51**, 325–350.

Honjo G., Kitamura N. & Mihama K. (1954) A study of clay minerals by means of single-crystal electron diffraction diagrams – the structure of tubular kaolin. *Clay Minerals Bulletin*, **4**, 133–141.

Honjo G. & Mihara K. (1954) A study of clay minerals by electron-diffraction diagrams due to individual crystallites. *Acta Crystallographica*, **7**, 511–513.

Inoue A., Utada M. & Natta T. (2012) Halloysite-to-kaolinite transformation by dissolution and recrystallization during weathering of crystalline rocks. *Clay Minerals*, **47**, 373–390.

Joussein E. (2016) Geology and mineralogy of nanosized tubular halloysite. Pp. 12–48 in: *Nanosized Tubular Clay Minerals, Halloysite and Imogolite* (P. Yuan, A. Thill & F. Bergaya, editors). Elsevier, Amsterdam, The Netherlands.

Joussein E., Petit S., Churchman J., Theng B., Righi D. & Delvaux B. (2005) Halloysite clay minerals – a review. *Clay Minerals*, **40**, 383–426.

Keeling J.L. (2015) The mineralogy, geology and occurrences of halloysite. Pp. 95–115 in: *Natural Mineral Nanotubes* (P. Pasbakhsh & G.J. Churchman, editors). Apple Academic Press, Oakville, Ontario, Canada.

Kogure T. & Inoue A. (2005) Determination of defect structures in kaolin minerals by high-resolution transmission electron microscopy (HRTEM). *American Mineralogist*, **90**, 85–89.

Kogure T., Johnston C.T., Kogel J.E. & Bish D. (2010) Stacking disorder in a sedimentary kaolinite. *Clays and Clay Minerals*, **58**, 63–72.

Kogure T., Mori K., Kimura Y. & Takai Y. (2011) Unraveling the stacking structure in tubular halloysite using a new TEM with computer-assisted minimal-dose system. *American Mineralogist*, **98**, 1776–1016.

Kogure T., Mori K., Drits V.A. & Takai Y. (2013) Structure of prismatic halloysite. *American Mineralogist*, **98**, 1008–1780.

Kohyama N., Fukushima K. & Fukami A. (1978) Observation of hydrated from of tubular halloysite by an electron microscope equipped with an environmental cell. *Clays and Clay Minerals*, **26**, 25–40.

Lvov Y.M., Schukin D.G., Mohwald H. & Price R.R. (2008) Halloysite clay nanotubes for controlled release of protective agents. *ACS Nano*, **2**, 814–820.

Matusik J., Gawel A.Bielanska E., Osuch W. & Bahranowski K. (2009) The effect of structural order on nanotubes derived from kaolin-group minerals. *Clays and Clay Minerals*, **57**, 452–464.

Moon V.G., Lowe D.J., Cunningham M.J., Wyatt J., Churchman G.L., de Lange W.P., Mörz T., Kreiter S., Kluger M.O. & Jorat M.E. (2015) Sensitive pyroclastic-derived halloysitic soils in northern New Zeland: interplay of microstructure, minerals, and geomechanics. Pp. 3–21 in: *Volcanic Rocks and Soils. Proceedings of the International Workshop on Volcanic Rocks and Soils, LaccoAmeno, Ischia Island, Italy* (T. Rotonda, M. Cecconi, F. Silvestri & P. Tommasi, editors). Taylor & Francis, London, UK.

Newman R.H., Childs C.W. & Churchman G.J. (1994) Aluminium coordination and structural disorder in halloysite and kaolinite by ^{27}Al NMR spectroscopy. *Clay Minerals*, **29**, 305–312.

Pasbakhsh P., Churchman G.J. & Keeling J.L. (2013) Characterisation of properties of various halloysites relevant to their use as nanotubes and microfiber fillers. *Applied Clay Science*, **74**, 47–57.

Plançon A., Giese R.F., Snyder R., Drits V.A. & Bookin A.S. (1989) Stacking faults in the kaolin-group mineral-defect structures of kaolinite. *Clays and Clay Minerals*, **37**, 203–210.

Reynolds R.C. (1986) The Lorentz-polarization factor and preferred orientation in oriented clay aggregates. *Clays and Clay Minerals*, **34**, 359–367.

Robertson I.D.M. & Eggleton R.A. (1991) Weathering of granitic muscovite to kaolinite and halloysite and of plagioclase-derived kaolinite to halloysite. *Clays and Clay Minerals*, **39**, 113–126.

Sakharov B.A. & Lanson B. (2013) X-ray identification of mixed-layer structures. Modelling of diffraction effects. Pp. 51–135 in: *Handbook of Clay Science, Part B. Techniques and Applications*, 2nd edition (F. Bergaya & G. Lagaly, editors). Elsevier, Amsterdam, Boston, Heidelberg, London, New York, Oxford.

Sakharov B.A., Drits V.A., McCarty D.K. & Walker G.M. (2016) Modeling of powder X-ray diffraction patterns of the Clay Minerals Society kaolinite standards: KGa-1b and KGa-2. *Clays and Clay Minerals*, **64**, 314–333.

Samotoin N.D. (2011) Enantiomorphism of kaolinite: observation on the level of individual kaolinite layer of the structure and on microcrystals. *Kristallography*, **56**, 353–361 (in Russian).

Shchukin D.G., Sukhorukov G.B., Price R.R. & Lvov Y. M. (2015) Halloysite nanotubes as biomimetic nanoreactors. *Small*, **1**, 510–513.

Singh B. (1996) Why does halloysite roll? A new model. *Clays and Clay Minerals*, **44**, 191–196.

Singh B. & Gilkes R.J. (1992) An electron optical investigation of the alteration of kaolinite to halloysite. *Clays and Clay Minerals*, **40**, 212–219.

Singh B. & Mackinnon (1996) Experimental transformation of kaolinite to halloysite. *Clays and Clay Minerals*, **44**, 825–834.

Wilson I.R. & Keeling J.L. (2016) Global occurrence and geology of halloysite. *Clay Minerals*, **51**, 309–324.

Yuan P., Tan D. & Annabi-Bergaya F. (2015) Properties and applications of halloysite nanotubes: recent research advances and future prospects. *Applied Clay Science*, **112–113**, 75–93.

Zvyagin B.B. (1964) *Electron Diffraction Analysis of Clay Mineral Structures*. Nauka, Moscow, Russia (in Russian).

Zvyagin B.B. (1967) *Electron Diffraction Analysis of Clay Mineral Structures*. Plenum Press, New York, NY, USA.